

Optical and infrared emission of H II complexes as a clue to the PAH life cycle

M. S. Khramtsova^{1*}, D. S. Wiebe¹, T. A. Lozinskaya², O. V. Egorov²

¹ *Institute of Astronomy, Russian Academy of Sciences, Pyatnitskaya str. 48, Moscow 119017, Russia*

² *Lomonosov Moscow State University, Sternberg Astronomical Institute, 13 Universitetskij prospekt, Moscow 119234, Russia*

14 August 2018

ABSTRACT

We present an analysis of optical spectroscopy and infrared aperture photometry of more than 100 H II complexes in nine galaxies. Spectra obtained with the 6-m telescope of SAO RAS are used along with archival data from *Spitzer* and several ground-based telescopes to infer a strength of polycyclic aromatic hydrocarbon (PAH) emission, age, properties of the UV radiation field, and metallicity of studied H II complexes. Physical properties (age, radiation field parameters, metallicity) are related to the F_8/F_{24} ratio used as a proxy for the PAH abundance in order to reveal factors that may influence the PAH evolution in H II complexes. The well-known correlation between the F_8/F_{24} ratio and metallicity is confirmed in the studied complexes. The infrared flux ratio also correlates with the $[\text{O III}]\lambda 5007/\text{H}\beta$ ratio which is often considered as an indicator of the radiation field hardness, but this correlation seems to be a mere reflection of a correlation between $[\text{O III}]\lambda 5007/\text{H}\beta$ and metallicity. In separate metallicity bins, the F_8/F_{24} ratio is found to correlate with an age of an H II complex, which is estimated from the equivalent width of H β line. The correlation is positive for low metallicity complexes and negative for high metallicity complexes. Analysing various mechanisms of PAH formation and destruction in the context of found correlations, we suggest that PAH abundance is likely altered by the UV radiation within H II complexes, but this is not necessarily due to their destruction. If PAHs can also form in H II complexes due to some processes like aromatisation, photodestruction, shattering and sputtering of very small grains, the net F_8/F_{24} ratio is determined by a balance between all these processes that can be different at different metallicities.

Key words: infrared: galaxies – ISM

1 INTRODUCTION

The tiniest dust particles, polycyclic aromatic hydrocarbons (PAHs), play a crucial role in the evolution of the interstellar medium (ISM). They are an important ingredient in astrochemical reactions, in particular, catalysing H₂ formation (Le Page, Snow & Bierbaum 2009) and enriching the ISM with simple organic species, being destroyed in photodissociation regions (PDRs) (Pety et al. 2005). They absorb UV-emission and heat gas via photoelectric effect. However, the genesis of these particles is still far from being understood. It is generally believed that PAHs are synthesised in hot dense outflows (~ 1000 K) of carbon-rich AGB stars (Gail & Sedlmayr 1987; Latter 1991; Cherchneff, Barker & Tielens 1992; Dhanao & Rawlings 2014) or in novae (Bode & Evans 2008). While theoretical calculations apparently confirm this

possibility, firm observational evidence is still scarce. PAHs are not seen in the vicinity of AGB stars, except for a few cases when their emission is observed in AGB stars with hot companions (Boersma, Hony & Tielens 2006). The weak PAH emission of AGB stars without companions is probably explained by insufficient UV irradiation that is needed to excite PAHs. However PAHs are often observed in planetary nebulae (Ryter 1991; Guzman-Ramirez et al. 2011) that represent a later stage of AGB star evolution. On the other hand, it was proposed in a number of works (Li & Draine 2002; Mattioda, Hudgins & Allamandola 2005) that some PAHs can be excited even by UV-poor radiation field. If this is the case, the lack of PAHs emission close to AGB stars becomes an issue in the origin of these particles.

Even though some PAHs along with other dust types can be synthesised in AGB stars, this process may not be sufficient to produce all the dust, especially small grains, observed in our Galaxy and in other galaxies. For example, Matsuura et al. (2009) and Matsuura, Woods & Owen

* E-mail: khramtsova@inasan.ru

(2013) showed that enrichment of the ISM by AGB stars in the LMC and SMC fails to explain the total dust and PAH abundance in these galaxies. PAH destruction in the ISM is apparently so effective (Micelotta, Jones & Tielens 2010a,b, 2011) that they do not survive the travel from parent stars to H II complexes where they are observed. The misbalance between the dust formation and destruction has also been noted for our Galaxy by Jones et al. (1994) and Jones, Tielens & Hollenbach (1996) (see however Jones & Nuth 2011). A conventional explanation is that some dust formation in molecular clouds is possible. A few mechanisms were suggested to explain PAHs and/or PAH precursors formation in cold molecular clouds (Greenberg et al. 2000; Parker et al. 2012). Some PAHs can also make it into interiors of H II complexes after having been formed in protoplanetary disks (Woods & Willacy 2007; Everett & Churchwell 2010).

A reverse process is also possible: PAHs may be a product of destruction of larger particles. Asano et al. (2013) and Hirashita & Kobayashi (2013) considered shattering process in the ISM as the main route to formation of small grains in galaxies. Besides shattering, other destruction mechanisms like sputtering, can be effective for larger particles in some circumstances. While gas sputtering works in hot plasma of supernova remnants at temperatures $> 10^5$ K (Draine & Salpeter 1979), alternative processes like chemical sputtering can be at work at lower temperatures (Salonen 2002). Jones et al. (2013) has shown that amorphous carbonaceous grains can become aromatised under the influence of UV radiation. Finally, in H II complexes and in PDRs formation of PAHs through UV evaporation of larger carbonaceous grains can be significant (Berné et al. 2007; Pilleri et al. 2012).

It is now well established that abundance of PAHs correlates with the metallicity of the environment where the PAH emission is observed (e.g. Draine et al. 2007; Smith et al. 2007; Wu et al. 2007; Hunt et al. 2010). Two typical explanations relate this correlation either to metallicity-dependent formation (Galliano, Dwek & Chantal 2008) or to metallicity-dependent destruction (Madden 2000). It has been shown in a number of studies that the correlation between the PAH abundance and metallicity holds not only globally, for a galaxy as a whole, but also locally, for individual H II complexes within the same galaxy (Gordon et al. 2008; Wiebe, Egorov & Lozinskaya 2011; Khramtsova et al. 2013). This apparently indicates that the mechanism, responsible for the correlation, operates *in situ*, in the same locations where PAHs are observed. In this case it seems reasonable to expect a certain connection between the PAH abundance and the region age. Slater et al. (2011) studied PAH emission from classical H II regions and superbubbles in the Large Magellanic Cloud and found no correlation between the emission properties and the morphology of an H II complex despite significant differences in ionization conditions. They concluded that whatever dust processing occurs in H II complexes it operates on a timescale that is either much shorter or much longer than the H II complex evolutionary timescale.

In the work of Khramtsova et al. (2013) we performed an aperture photometry of about 200 star-forming complexes in 24 galaxies to find correlations between PAH emission properties. A local character of the PAH-metallicity cor-

relation and an apparent anti-correlation between the PAH abundance and radiation field led us to conclude that the ‘destructive’ scenario is a preferred one. However, to put any conclusion on the PAH evolution in H II complexes on a more solid ground, a comparison with ages would be helpful.

In this work we attempt to relate the PAH content in extragalactic H II complexes to their metallicity, shape of the ionizing UV field spectrum, and age. The correlations or a lack of thereof between the F_8/F_{24} ratio and physical parameters of H II complexes like an age and ionizing UV field strength may be a key to understand the formation and destruction of the PAHs. Specifically, if we give a preference to a ‘destructive’ scenario, we might expect that the PAH content decreases with age in H II complexes, and if PAHs are destroyed more effectively by harder radiation, we might also expect that the PAH content decreases faster when radiation field hardness is greater.

The structure of the paper is the following. In Section 2 we present observational data that are used in our analysis. In Section 3 we describe how physical parameters of H II complexes are estimated from these data and also comment on the reliability of our estimates. In Section 4 we provide correlations between estimated parameters of H II complexes and discuss their relation to the problem of the PAH evolution in Section 5.

2 DATA

In this Section we present observational data on the optical spectroscopy of extragalactic H II complexes used to derive their metallicities, ages, and radiation field properties and infrared data used to perform the aperture photometry of the same complexes.

2.1 Sample

We present results based on investigations of H II complexes in nine galaxies. The sample was chosen to probe a correlation of F_8/F_{24} ratio with parameters of H II complexes in a wide range of metallicities. We obtained own observations for two galaxies, NGC 7741 and IC 1727, that represent low and high ends of the galactic metallicity distribution. Their spectroscopic observations are presented in this work for the first time. To make the sample representative we expanded it with seven more galaxies. These galaxies have different morphological types, metallicities and are included in the SINGS survey. Also, they were studied in our previous work (Khramtsova et al. 2013). There are other SINGS galaxies with spectroscopic data available, however, they all have quite high metal content. We have tried to make the sample as uniform as possible and not to bias the sample towards high metallicity galaxies. Spectroscopic data for H II complexes in the added seven galaxies were taken from the literature. In total, we found spectroscopic data for 199 complexes in considered galaxies. Due to a lower resolution and insufficient sensitivity of IR images not all complexes studied spectroscopically can be measured photometrically on IR images. We include in the final sample only those H II complexes that both have spectroscopic observations available and can be detected and measured with sufficient signal-to-noise ratio ($S/N > 3$ at $8\mu\text{m}$) on IR images. Ninety com-

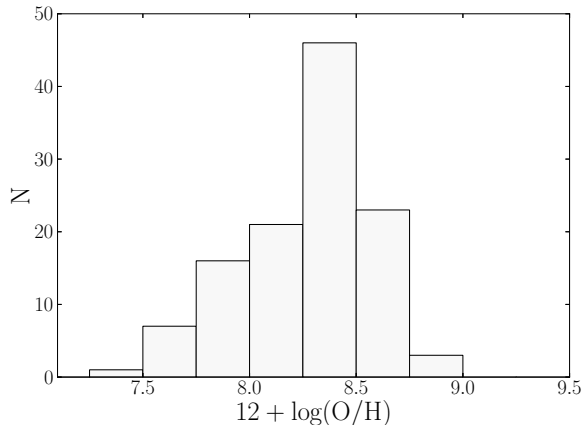


Figure 1. A metallicity distribution of studied H II complexes. Metallicities were estimated by the ‘ONS’-method (Pilyugin, Vílchez & Thuan 2010).

plexes, mostly of small angular size, which have been observed spectroscopically, but cannot be resolved or are too weak on IR images, were excluded from the sample. They have nearly the same age and metallicity distributions as the remaining complexes and, thus, their exclusion does not introduce any strong bias into the sample.

Altogether the current sample includes 109 H II complexes (including newly observed complexes in IC 1727 and NGC 7741). The information about the number of H II complexes studied in each galaxy along with the distance to the galaxy, its morphological type and a source of optical spectroscopic data (with corresponding references) is presented in Table 1. The number of complexes in IC 1727 and NGC 7741 that have been studied only spectroscopically (see above) is shown in parentheses.

The entire sample covers a wide range of metallicities from the lowest values of the order of 7.5–7.9 (complexes in Holmberg II) to solar or super-solar values, around 8.6–8.8 (e.g. NGC 3184). It allows studying how physical properties change over the transition from low to high metallicity environments. A metallicity distribution for our sample is shown in Fig. 1.

The nearest galaxy in the sample is Holmberg II that belongs to the M81 group at a distance of about 3.4 Mpc (Jacobs et al. 2009). The most remote is NGC 7741, with distance estimates ranging from 12.1 to 17.5 Mpc (Willick et al. 1997) and the most recent measurements being 15.1 Mpc (Tully et al. 2009). Therefore a typical aperture size of 6'' for NGC 7741 corresponds to the linear size of about 500 pc, while a 10'' aperture for the closest galaxy of the sample, Holmberg II, corresponds to ~ 200 pc.

2.2 Spectroscopic Data

Spectroscopic observations of H II complexes in IC 1727 and NGC 7741 galaxies were performed with the 6-m telescope of the Special Astrophysical Observatory of the Russian Academy of Sciences (SAO RAS) using the multi-mode SCORPIO focal reducer (Afanasiev & Moiseev 2005) in the long-slit spectroscopy mode on 22–23 of October, 2011. The used slit has length of 6' and width of 1''. In Fig. 2 we show

images of IC 1727 and NGC 7741 galaxies in H α passband. Locations of slits and studied H II complexes are also indicated. The complexes studied both spectroscopically and photometrically are marked by black circles, while red circles correspond to complexes studied only spectroscopically. We used VPHG550G grism and EEV CCD42-40 CCD detector with the 3700–7300Å wavelength range that covers all the important nebular emission lines. The spectral resolution is 10Å and dispersion is 2.1Å/pix, which is sufficient for our goal of abundance and age estimating. Exposure time, 15 min, was the same for all spectra. The number of exposures for one slit location is 4. Seeing during observations varied from 0.8'' to 1.1''.

Spectra were reduced with a standard procedure that includes the bias field subtraction, normalization by flat fields, wavelength calibration, sky lines subtraction, and flux calibration using spectrophotometric standards GD 93-48 and AGK+81d266. All steps were performed with the IDL software developed at the SAO RAS specifically for long-slit data. Emission lines were fitted by a single or multiple gaussians. [N II] $\lambda\lambda$ 6548, 6584 and H α lines were measured using a triple gaussian. Spectra were corrected for the interstellar extinction using the average decrement from the ratios of Balmer lines H α /H β and H γ /H β when it is possible or H α /H β only if H γ is too weak. Theoretical values for these ratios, 2.86 and 0.47, correspondingly, were taken from Osterbrock & Ferland (2006) for $T_e \approx 10000$ K. We calculated colour excess E(B–V) using the extinction curve from the work of Cardelli, Clayton & Mathis (1989) and parameterization from the work of Fitzpatrick (1999). Examples of typical spectra for H II complexes in these galaxies are presented in Fig. 3. We measured equivalent widths with the stellar continuum, while to measure line intensities, we subtracted it using the open software ULYSS¹, though stellar contribution for studied complexes is almost negligible and does not affect results noticeably.

The list of H II complexes and results of the spectroscopy for IC 1727 and NGC 7741 galaxies are presented in Table 2. The offsets are given relative to the centre of the galaxy (positive values are toward the East and the North). The equatorial coordinates of IC 1727 and NGC 7741 centres, adopted from Saintonge et al. (2008), are $\alpha = 01^h 14^m 29.90^s$, $\delta = +27^\circ 19' 58.0''$ and $\alpha = 23^h 43^m 54.5^s$, $\delta = +26^\circ 04' 31.0''$, respectively. Position angle PA = 150°, inclination $i = 68^\circ$, and radius at 25 mag in the B band $R_{25} = 193''$ for IC 1727 are taken from Epinat, Amram & Marcelin (2008). Parameters for NGC 7741 are taken from the HyperLeda galactic database² (Paturel et al. 2003): PA = 153.5°, $i = 50.2^\circ$, and $R_{25} = 108.9''$. Table 2 includes the offsets relative to centres of galaxies, bright line intensities, normalised to H β intensity, colour excesses, metallicities, and radial distances of H II complexes. Methods of metallicity estimation are described below.

Spectra of H II complexes in Holmberg II were also obtained with the 6-m telescope of the SAO RAS and presented in the work of Egorov, Lozinskaya & Moiseev (2013). We used their spectra to measure an equivalent width of the H β line and adopted their estimations of metal-

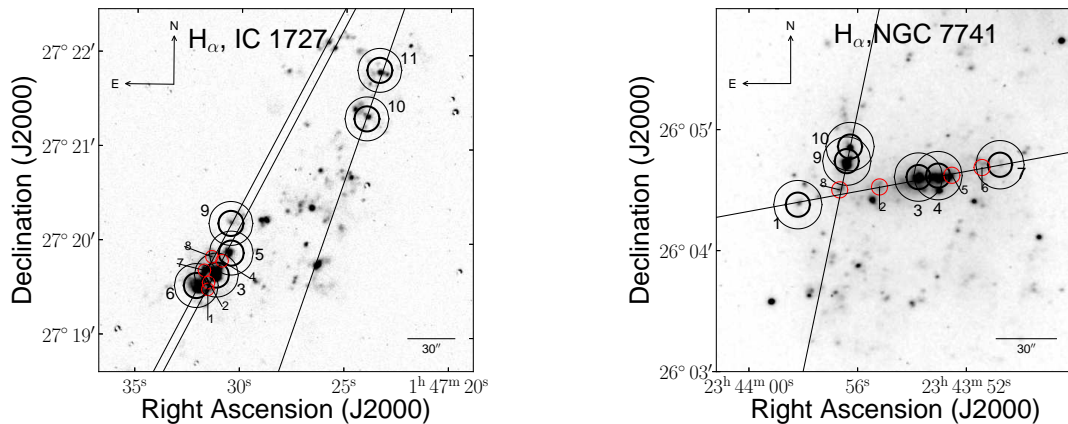
¹ <http://ulyss.univ-lyon1.fr/>

² <http://leda.univ-lyon1.fr>

Table 1. Summary of galaxies included in the work: name, number of studied H II complexes, adopted distance and its reference source, morphological type and reference sources for optical spectroscopic data.

Name	Number of H II complexes	Distance, Mpc [ref.]	Morphological type	ref.
IC 1727	6 (11)	6.8 [1]	SB(s)m	this work
NGC 7741	6 (10)	15.1 [1]	SBc	this work
Holmberg II	12	3.4 [3]	Im	[6]
IC 2574	11	3.8 [4]	SAB(s)m	[7]
NGC 628	10	7.3 [2]	Sc	[8,9]
NGC 925	18	9.3 [2]	Scd	[9]
NGC 3184	11	11.1 [5]	SABc	[9]
NGC 3621	21	6.7 [2]	SBcd	[10]
NGC 6946	14	5.9 [2]	SABc	[11]

References: (1) Tully et al. (2009), (2) Karachentsev et al. (2004), (3) Jacobs et al. (2009), (4) Dalcanton et al. (2009), (5) Leonard et al. (2002), (6) Egorov, Lozinskaya & Moiseev (2013), (7) Croxall et al. (2009), (8) Gusev et al. (2012), (9) van Zee et al. (1998), (10) Ryder (1995), (11) Gusev, Sakhibov & Dodonov (2013)

**Figure 2.** $H\alpha$ images of IC 1727 (left) and NGC 7741 (right) galaxies with locations of slits and H II complexes. Red circles represent H II complexes studied only spectroscopically. Black circles indicate complexes studied both spectroscopically and photometrically. Thick black circles indicate areas for performing photometry, while thin black circles show regions used for background subtraction.

licity. Spectroscopy data (line intensities and $EW(H\beta)$) for IC 2574 are taken from Croxall et al. (2009), data for NGC 628 are partly from Gusev et al. (2012) and partly from van Zee et al. (1998), data for NGC 6946 are taken from Gusev, Sakhibov & Dodonov (2013), and NGC 925 and NGC 3184 data are taken from van Zee et al. (1998). Finally, NGC 3621 data are from Ryder (1995). We calculate metallicities and ages of H II complexes using these data.

2.3 Infrared photometry

We perform the aperture photometry for H II complexes in all nine galaxies using the *Spitzer* data at wavelengths of 3.6, 4.5, 5.8 and 8.0 μm (the IRAC instrument) and 24 μm (the MIPS instrument). IC 1727 and NGC 7741 data were downloaded from the Spitzer Data Archive³. Other galaxies belong to the SINGS sample (Kennicutt et al. 2003),

and we downloaded the reduced images from the SINGS project website⁴. Prior to performing the aperture photometry we convolved images to a MIPS resolution at 24 μm (6'') with the IDL convolution procedure and kernels provided by Aniano et al. (2011). Also, we rescaled images to make pixel sizes equal to 1.5'' for all images.

We sum fluxes of pixels within chosen apertures subtracting an average background level in a surrounding ring adjacent to an aperture (width of a ring is $\sim 6''$). Note that we do not apply the IRAC extended source correction factors considering H II complexes as point sources. Since we convolve images to matched point spread functions (PSF), we do not need to use IRAC or MIPS aperture corrections. Examples of apertures (thick circles) and background rings (thin circles) are demonstrated in Fig. 2 for complexes in IC 1727 and NGC 7741. Contributions of bright pixels (three times brighter than the standard deviation in a ring, σ_{ring}) in a background area are ignored to avoid overestimating. These pixels can be related to neighbouring complexes. The

³ <http://sha.ipac.caltech.edu>

⁴ <http://sings.stsci.edu>

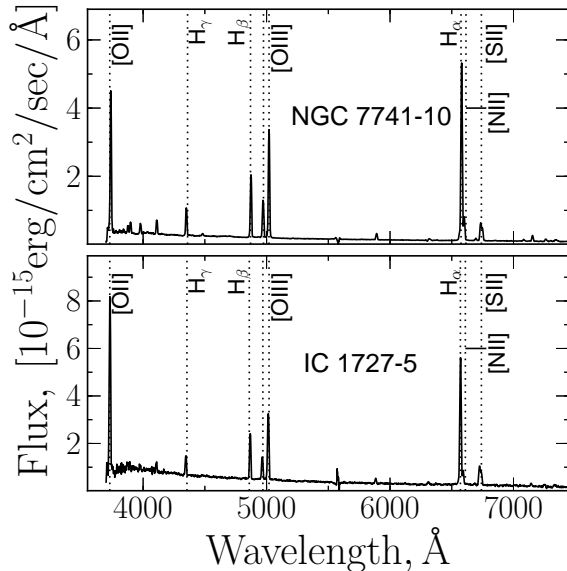


Figure 3. Typical spectra of H II complexes in NGC 7741 and IC 1727 galaxies obtained with the 6-m telescope of the SAO RAS. Bright emission lines used for further analysis are marked on the spectra.

total error of an aperture flux consists of the background noise level (σ_{ring}) and an error due to the shift of an aperture centre σ_{pos} that can be comparable to the first error. We do not take into account a beam size correction in measurements. The same method was used in our previous work (Khramtsova et al. 2013), and more details can be found there.

It must be noted that our technique to compute σ_{ring} likely leads to an underestimate of the noise, since our pixels are smaller than the beam, and adjacent pixels are likely correlated. This does not affect our conclusions, as σ_{ring} is not used in the computations directly, serving only as a tool to avoid pixels belonging to neighbouring complexes. But still, uncertainties in Table 3 can actually be somewhat larger because of this.

It is believed that $8 \mu\text{m}$ emission arises mostly from vibrational modes of PAHs, and $24 \mu\text{m}$ emission mostly represents thermal emission of hot very small grains (VSGs) (e.g. Draine & Li 2007). However, the exact contributions of PAHs to the $8 \mu\text{m}$ emission and VSGs to the $24 \mu\text{m}$ emission may vary from an object to an object depending on a number of factors (e.g. on metallicity). Actually, thermal emission can contribute at $8 \mu\text{m}$ as well (Engelbracht et al. 2005), and PAH emission can constitute a substantial fraction of emission at $24 \mu\text{m}$ (Robitaille et al. 2012). Stars and dust continuum from larger dust grains can contribute at these wavelengths as well. We estimated aromatic feature emission (‘afe’) at $8 \mu\text{m}$ and flux with subtracted stellar continuum (‘ns’) at $24 \mu\text{m}$ as suggested in the work of Marble et al. (2010). Note that throughout the paper we use shorter designation F_8/F_{24} that actually means $F_8^{\text{afe}}/F_{24}^{\text{ns}}$.

Photometry results are presented in Table 3 that includes a designation of a complex (column 1), equatorial coordinates on the Spitzer images (columns 2,3), aperture radius (column 4), measured fluxes at 3.6, 4.5, 5.8, $8.0 \mu\text{m}$, con-

tribution from aromatic features at $8.0 \mu\text{m}$, measured flux at $24 \mu\text{m}$ and flux without the stellar contribution at $24 \mu\text{m}$ (columns 5-11). Designations of complexes for IC 1727 and NGC 7741 are the same as in Table 2. Some of the complexes that we observed spectroscopically in NGC 7741 and IC 1727 are not resolved in Spitzer images, so no photometry for them is presented in Table 3. Region designations for other galaxies were taken from the corresponding references with spectroscopic measurements.

3 PHYSICAL PARAMETERS OF H II COMPLEXES

The goal of this study is to check whether correlations exist between the H II complex properties and their PAH content. In particular, it is interesting to see if PAH evolution is somehow related to the radiation field properties in various environments. It has been proposed that harder radiation field in lower metallicity medium can be an underlying reason for the observed correlation between metallicity, $12 + \log(\text{O}/\text{H})$, and the PAH mass fraction, q_{PAH} . If PAHs are indeed destroyed faster by harder photons, at a given age we may expect less PAHs in an H II complex with harder radiation field. Optical spectra presented in the previous Section allow estimating physical parameters of the studied H II complexes, first of all, their metallicities and ages. Also, ratios between some spectral line intensities may depend on the hardness of ionizing field. Below we describe how we estimate these parameters, present our results that are summarised in Table 4, and also provide some comments on their reliability.

3.1 Abundance of PAHs

According to the dust emission model by Draine & Li (2007), the PAH mass fraction, q_{PAH} , in the total dust mass can be estimated, provided far-infrared fluxes are known for the studied region at least up to $160 \mu\text{m}$. This implies usage of *Herschel* data. However, most star-forming complexes we analyse are located in crowded environments so that *Herschel* angular resolution is not sufficient to study them separately from neighbouring regions. Thus, we limit ourselves with *Spitzer* data and use the F_8/F_{24} ratio as a tracer of the PAH abundance.

In our previous work we showed that F_8/F_{24} ratio correlates with q_{PAH} (Khramtsova et al. 2013). Similar conclusions were reached by Sandstrom et al. (2010) and Engelbracht et al. (2005) though the scatter can be significant, for example, because of differences in starlight fields.

The F_8/F_{24} ratio is not a direct measure of q_{PAH} as it does not contain information on the cold dust component consisting of big grains (BGs). Nevertheless, we believe that the ratio can be used as a tracer of the PAH content for following reasons. According to Draine & Li (2007), the fraction of $8 \mu\text{m}$ emission in the total infrared flux sensitively depends on q_{PAH} , while the relative intensity of the $24 \mu\text{m}$ emission is only weakly dependent on the PAH content, and this dependence becomes even less pronounced for the radiation field parameter U greater than ten (U is the minimum starlight intensity in the complex in units of the interstellar radiation field in the Sun’s vicinity), which is expected in

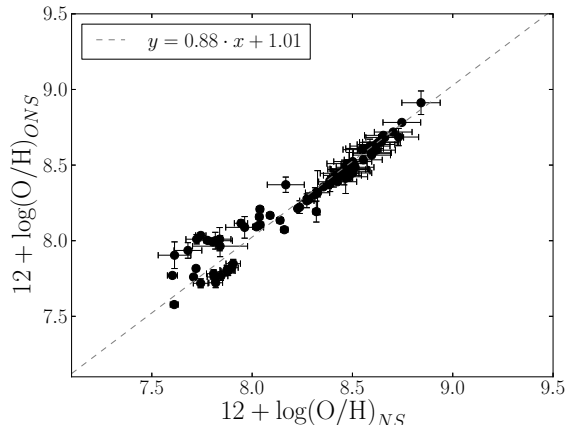


Figure 4. Comparison between the two metallicity estimation methods (NS and ONS) used in this work. The dotted line indicates the linear fit for this comparison. The corresponding equation is also shown.

star-forming regions. Apparently, the $24\ \mu\text{m}$ emission ratio to the emission of colder BGs is relatively constant for objects in our sample. Therefore F_8/F_{24} ratio is equivalent to ratio of F_8 to the total infrared flux. Consequently, the ratio of $8\ \mu\text{m}$ and $24\ \mu\text{m}$ fluxes should reflect the PAH content reliably.

3.2 Metallicities

A number of methods have been developed over the years to estimate metallicity of H II regions. It is believed that the most direct way to estimate metallicity is through the use of electron temperature T_e (Stasińska 2004). To apply this method, an [O III] λ 4363 line is usually used. However, in most cases it is quite weak, so other methods that require only bright lines were proposed as alternatives to the ‘direct’ one. They can be separated into empirical (Pilyugin & Thuan 2005; Pilyugin, Vílchez & Thuan 2010; Pilyugin & Mattsson 2011, etc.) and theoretical (e.g., Kobulnicky & Kewley 2004) groups. A comparison of various methods and their relation to the ‘direct’ method were studied extensively (Kewley & Ellison 2008; López-Sánchez et al. 2012; Egorov, Lozinskaya & Moiseev 2013).

We prefer to use a so-called ‘ONS’ method based on the measurements of bright oxygen ([O II] λ 3727, 3729, [O III] λ 4959, 5007), nitrogen ([N II] λ 6548, 6584), and sulfur ([S II] λ 6717, 6731) lines (Pilyugin, Vílchez & Thuan 2010). In Holmberg II data on the [O II] λ 3727, 3729 lines are not available except for a couple of complexes, so we rely on the ‘NS’ calibration (Pilyugin & Mattsson 2011) to estimate metallicities in this galaxy. These two calibrations are close to each other as shown in the work of Egorov, Lozinskaya & Moiseev (2013). We compared the NS and ONS metallicity estimates for the rest of our sample of H II complexes and found them to be consistent with each other. This is illustrated in Fig. 4. The linear fit line is also shown.

Diagrams showing radial metallicity profiles in IC 1727 and NGC 7741 galaxies are presented in Fig. 5.

H II complexes in disk galaxies typically demonstrate a metallicity gradient (Vila-Costas & Edmunds 1992; Zaritsky, Kennicutt & Huchra 1994; van Zee et al. 1998). This gradient is clearly seen in the NGC 7741 galaxy. A slope of a gradient likely depends on the galaxy morphological type and becomes steeper in late-type galaxies (Oey & Kennicutt 1993; Zaritsky, Kennicutt & Huchra 1994). Unlike disk galaxies, SB(s)m galaxies are not expected to have a noticeable gradient, and indeed nearly flat oxygen abundance distribution is seen in IC 1727. Gradients for other galaxies in our sample have been presented in their respective studies except for Holmberg II and IC 2574 where the gradient is not expected, in particular, because of rather compact location of studied H II complexes.

3.3 Ages

We estimate ages of H II complexes using $EW(H\beta)$. In a case of a single stellar population formed in an instantaneous star formation burst, $EW(H\beta)$ has a maximum at the onset of the star formation and then gradually decreases with time. This method was originally suggested by Copetti, Pastoriza & Dottori (1986) and later discussed by Schaerer & Vacca (1998) and Stasińska & Leitherer (1996). Levesque et al. (2010) gave some expressions to determine the burst age for different metallicities ($Z/Z_\odot = 0.05, 0.2, 0.4, 1.0, 2.0$). We use these expressions to estimate ages of H II complexes with calibrations for an appropriate metallicity, even though an assumption of a single stellar population may not be strictly valid. If stellar populations of different ages coexist in the same H II complex (Bresolin, Kennicutt & Garnett 1999; Peacock, Zepf & Finzell 2013), older stars can make a significant contribution to the continuum, correspondingly decreasing $EW(H\beta)$. This can lead to an age overestimation. In principle, multiple stellar populations can be traced by absorption lines and the increased slope of the spectra, but our spectra do not contain strong absorption lines, and the slopes are quite flat, so we use a single stellar population model to estimate ages of our H II complexes. Potentially, this can be a problem for NGC 7741 as this galaxy is located further away than other galaxies from our sample so that it is possible that some older stars that do not belong to H II complexes have been covered by the slit. In this case ages of these complexes are somewhat overestimated.

One possible source of uncertainty in our study is the potential inconsistency between metallicities that are used to derive the age calibration and metallicities estimated from spectral data. To estimate the role of this uncertainty, we utilize models presented by Levesque, Kewley & Larson (2010)⁵. These authors have used the Starburst99 code (Leitherer et al. 1999) to compute synthetic ionizing FUV radiation spectra as a function of metallicity, star formation history, and age. These spectra have then been used as an input for the Mappings III photoionization code (Sutherland & Dopita 1993; Groves, Dopita & Sutherland 2004) to compute (in particular) line intensity ratios.

We have used these line ratios to compute metallicities with NS and ONS calibrations. They turned out

⁵ Available at <http://www.emlevesque.com>

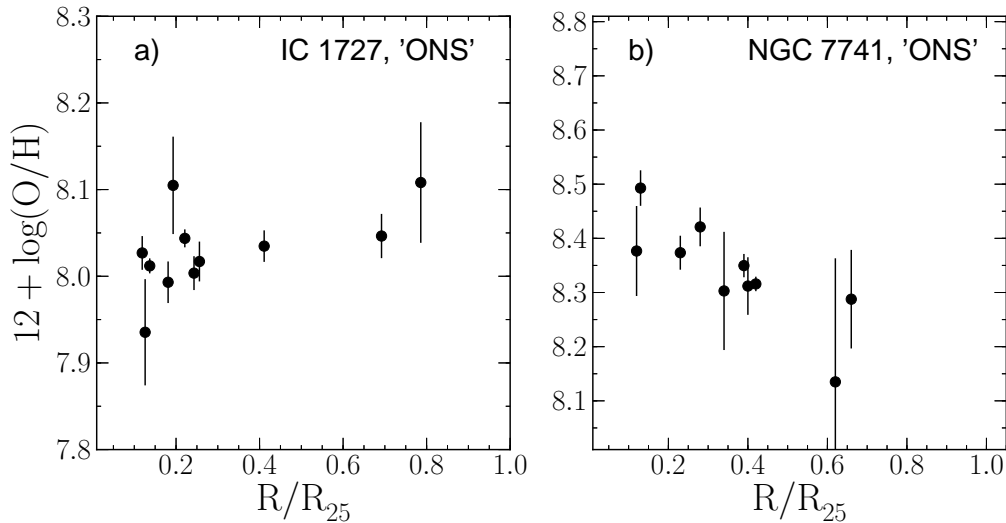


Figure 5. Metallicities vs. radial distances of H II complexes for IC 1727 and NGC 7741. Metallicities are estimated by the ONS method.

to be consistent with ‘true’ metallicities given in the Levesque, Kewley & Larson (2010) grid as input parameters. Inconsistency only appears in models with the lowest value of the ionization parameter (10^7 cm s^{-1} ; see the next subsection) and at ages greater than 5 Myr, where NS and ONS methods tend to give lower metallicities than the ‘true’ ones.

The similar analysis has been presented in the work of López-Sánchez et al. (2012). These authors have also shown that in the case of continuous star formation NS and ONS methods provide consistent, but underestimated metallicities. In order to check the significance of this underestimation, we have repeated all our computations with metallicities artificially increased by 0.5 dex (a typical discrepancy in the López-Sánchez et al. (2012) study) and found that none of our conclusions is affected by this change. So, to avoid confusion, we provide age values computed with the ONS (NS) metallicities.

Ages for some regions in IC 2574 and Holmberg II were estimated earlier in the works of Stewart & Walter (2000) and Stewart et al. (2000), correspondingly. Their method is based on the assumption of a single stellar population as well, but measurements FUV, B, and $H\alpha$ are used instead of $H\beta$. We compare our age estimates with ages presented in cited works in Fig. 6. In the work of Stewart et al. (2000) all complexes are separated into four groups by their ages. We illustrate these estimates by squares with error bars that show age ranges for each group. Circles represents ages of complexes in IC 2574 from Stewart & Walter (2000)⁶.

With the one exception, our results are consistent with previous estimates. The deviant point corresponds to an HSK61 complex in Holmberg II. This complex is quite extended, so it is possible that a spectrograph slit was located in a position with older populations. Also, weakness of emission in this complex might have led to incorrect results. The

kinematic age estimate for this region is only about 3.7 Myr (Wiebe et al. 2014). Otherwise, all age estimates are mainly in agreement.

Pellerin et al. (2012) presented some age estimates for complexes in IC 2574 using colour-magnitude diagram for resolved stars. They divided all stellar systems into three age groups, with clusters from the youngest group having ages less than 10 Myr. All our complexes fall into this group. Apparently, they do not contain significant older populations, and, thus, an assumption of a single stellar population is justified for complexes in IC 2574.

We have excluded the +085–042 region from NGC 3184 which has an exceptionally wide $H\beta$ line, according to van Zee et al. (1998), corresponding to age of 0.1 Myr. We believe this age value is unreliable as in other aspects the region does not differ from the older regions.

3.4 Radiation field hardness

PAHs and other dust grains are destroyed by UV radiation, and it is reasonable to assume that the greater the average photon energy, the more effective it is as a destruction factor. Thus, the rate of PAH photodissociation should depend on the radiation field hardness. Some line ratios, like $[O \text{ III}]\lambda 5007/H\beta$, $[S \text{ II}]\lambda 6717 + 6731/H\alpha$, $[Ne \text{ III}]/[Ne \text{ II}]$, are proposed as indicators of the shape of the radiation field spectrum. Line intensity ratios $[O \text{ III}]\lambda 5007/H\beta$ and $[S \text{ II}]/H\alpha$ have been proposed as tracers of the radiation field hardness by Levesque, Kewley & Larson (2010). Harder radiation increases O^{++} abundance, as it contains more photons able to ionize O^+ , and decreases S^+ abundance, as it penetrates deeper into the surrounding gas and produces more S^{++} ions. Thus, $[O \text{ III}]\lambda 5007/H\beta$ is expected to be an increasing function of the radiation field hardness, while $[S \text{ II}]/H\alpha$ should decrease in harder radiation field.

To verify if it is indeed the case, we use the pre-computed line ratios from the Levesque, Kewley & Larson (2010) grid and relate them to UV spectra properties. As the spectra themselves are not available in the published database, we have computed them using the

⁶ Note that in Table 2 from this paper the column with ages is actually a copy of the column with FUV luminosities. The authors provided us with the correct values of ages.

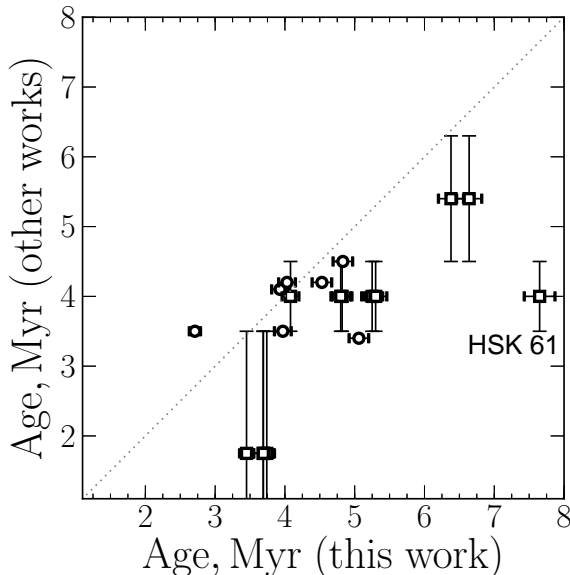


Figure 6. Comparison of age estimates from this work and from the works of Stewart & Walter (2000) and Stewart et al. (2000) for complexes in IC 2574 and Holmberg II. Squares with error bars correspond to complexes in Holmberg II. The real ages of complexes are contained within the ranges indicated by error bars and squares are just middle values for these ranges. Circles correspond to complexes in IC 2574.

Starburst99 code and the same parameter sets as in Levesque, Kewley & Larson (2010). Specifically, instantaneous star formation burst is used with the Geneva “Standard” mass-loss tracks (Schaller et al. 1992; Schaerer et al. 1993a,b; Charbonnel et al. 1993). Data for the electron density of 10^2 cm^{-3} are used.

Various definitions of the radiation field hardness (or alternatively softness) are described in the literature, like the starlight effective temperature (Vilchez & Pagel 1988) or the spectral index in the range from 1 to 4 rydberg (e.g., Kewley et al. 2001), often bound to the ionization state of certain elements. Our study is not directly related to the ionization structure of the complexes. Considering PAH destruction, we mostly need to know the overall energy distribution over hard and soft UV ranges. So, we define hardness as the ratio of integrated fluxes in the ranges from 90\AA to 912\AA and from 912\AA to 2000\AA . The intermediate value has no particular meaning and just separates the hard part of the spectrum that evolves significantly with time and the soft part of the spectrum longward of the Lyman limit that stays relatively constant. The adopted hardness measure, computed from the Starburst99 spectra, drops both with age and metallicity as shown in Fig. 7. The similar definition was suggested in the work of Leboutteiller et al. (2011) for the PAH destruction investigation.

The next step is to check whether the line ratios mentioned above can be used to trace the adopted hardness measure. An additional factor that enters the line ratio computation is the so-called ionization parameter q , which represents the ratio of the ionizing photon flux to the electron density (Osterbrock & Ferland 2006). In the work of Levesque, Kewley & Larson (2010) seven values of $q \approx 10^7$,

2×10^7 , 4×10^7 , 8×10^7 , 1×10^8 , 2×10^8 , and $4 \times 10^8 \text{ cm s}^{-1}$ are used, which bracket possible ionization parameter values in actual H II complexes.

In Fig. 8 we show how the $[\text{S II}]/\text{H}\alpha$, $[\text{O III}]\lambda 5007/\text{H}\beta$, and $[\text{Ne III}]/[\text{Ne II}]$ ratios are related to our hard-to-soft flux ratio. Black and red curves correspond to q values of 10^7 and $4 \times 10^8 \text{ cm s}^{-1}$, respectively. There is some anti-correlation between the spectrum hardness and the $[\text{S II}]/\text{H}\alpha$ ratio for the higher value of q , as seen on the top panel, however, any correlation is absent for the lower value of the ionization parameter. The correlation between the overall radiation field shape and the $[\text{O III}]\lambda 5007/\text{H}\beta$ and $[\text{Ne III}]/[\text{Ne II}]$ is much stronger, but apparently we need to estimate the ionization parameter in order to infer the radiation field hardness from the line ratios.

An ionization parameter in a particular H II complex depends on many parameters, both internal and external (e.g., Dopita et al. 2006). In principle, in our complexes it may take any value within the general limits indicated by observations of extragalactic H II regions. Levesque & Richardson (2014) have presented a parameterization of the $\log([\text{O III}]\lambda 5007/[\text{O II}]\lambda 3727)$ ratio as a diagnostic of the ionization parameter. Using their relation with the spectroscopic data we have collected and our metallicity estimates, we find that most of our regions have q below $4 \times 10^7 \text{ cm s}^{-1}$. Curves corresponding to this value of q are shown with blue colour in Fig. 8. Apparently, a ratio of neon infrared emission lines is the best tracer of the radiation field hardness, which was used in a number of works (e.g. Leboutteiller et al. 2011). The scatter in the $[\text{O III}]\lambda 5007/\text{H}\beta$ line ratios for a given value of the hard-to-soft flux ratio is quite significant even in the narrow q range from 10^7 cm s^{-1} to $4 \times 10^7 \text{ cm s}^{-1}$. This implies that when the hard-to-soft flux ratio is high (at low metallicity and/or in younger complexes), the uncertainty in its value can reach an order of magnitude, which is comparable to scatter in observed line ratios.

To conclude this section, in Fig. 9 we relate the observed $[\text{O III}]\lambda 5007/\text{H}\beta$ ratio to our derived H II complex metallicities and ages and compare it to the theoretical predictions. A top row shows that the line ratio is nearly independent of metallicity at $12 + \log(\text{O}/\text{H}) \lesssim 8.3$ and then decreases indicating that higher metallicity complexes mostly have softer radiation field. This is the same kind of behaviour that is predicted by theoretical models. Specifically, in panel Fig. 9a we show results of numerical modelling by Levesque, Kewley & Larson (2010) for various ages and ionization parameters as indicated in the legend.

The correlation of the $[\text{O III}]\lambda 5007/\text{H}\beta$ ratio with age is weaker (Fig. 9b). Note that there are few H II complexes that possess high $[\text{O III}]\lambda 5007/\text{H}\beta$ ratios at ages of the order of 6 Myr or greater, contrary to theoretical predictions. These are, probably, the complexes where the instantaneous star formation burst assumption is not valid.

Fig. 9 also hints at uncertainty in q estimates. Blue lines in Fig. 9a and Fig. 9b correspond to $q = 4 \times 10^7 \text{ cm s}^{-1}$, which is higher than average in our complexes according to parameterization from the work of Levesque & Richardson (2014). However, models with this q value predict lower $[\text{O III}]\lambda 5007/\text{H}\beta$ than in most considered complexes. In order to match theoretical predictions with observed values, $q \sim 10^8 \text{ cm s}^{-1}$ or greater is needed as indicated by green

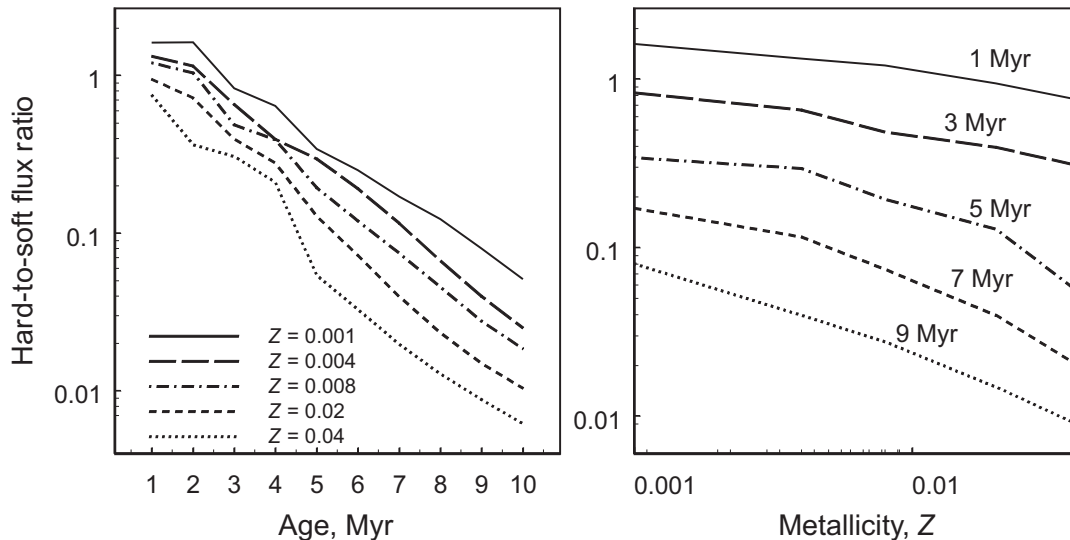


Figure 7. Evolution (left panel) and dependence on metallicity (right panel) of the hard-to-soft flux ratio that we adopt as a measure of the radiation field hardness. Different linestyles correspond to different metallicities on the left panel and to different ages on the right panel. Spectra are computed with the Starburst99 code.

lines in Fig. 9a Fig. 9b. Note that this discrepancy arises even though same observations and same model grids are used both in the $[\text{O III}]\lambda 5007/[\text{O II}]\lambda 3727$ parameterization and in Fig. 9. Levesque & Richardson (2014) used Geneva ‘high’-mass-loss stellar evolutionary tracks (Meynet et al. 1994) to derive their parameterization, but in Fig. 9 higher q values provide better match between theory and observations for both choices (‘standard’ or ‘high’) of evolutionary tracks. If q values of the order of 10^8 cm s^{-1} or higher are indeed wide-spread, the $[\text{O III}]\lambda 5007/\text{H}\beta$ as an indicator of the radiation field hardness becomes more reliable.

Summarising, all the considered theoretical line ratios ($[\text{S II}]/\text{H}\alpha$, $[\text{O III}]\lambda 5007/\text{H}\beta$, and $[\text{Ne III}]/[\text{Ne II}]$) show expected dependence on the radiation field hardness, but none of them is particularly useful for our purpose due to the uncertainties related to the ionization parameter.

4 RELATIONS BETWEEN VARIOUS PARAMETERS

Our ‘ideal’ object is a star-forming complex that has been formed in a single star formation event and since then progressively evolves into an H II complex. It is characterized by certain metallicity and by some initial PAH content that may or may not depend on metallicity. The oldest complex in our sample has age less than 10 Myr, so we do not expect to see any metallicity evolution. The initially abundant PAHs are destroyed by UV radiation, with harder photons being more destructive than softer photons. If the initial PAH abundance does not depend on metallicity, while their destruction rate depends on metallicity, we would expect the $12 + \log(\text{O}/\text{H}) - F_8/F_{24}$ correlation to be weaker (or absent) in younger complexes and to become stronger in older complexes. Also, we would expect the F_8/F_{24} ratio to become smaller with time if PAHs are destroyed more effectively than larger grains (Allain, Leach & Sedlmayr 1996). Our complexes have sizes of the order of a few hundred pc,

which is much bigger than the size of an individual H II region. However, this does not mean that processes we discuss operate on this spatial scale. What we observe is actually a merged result of dust evolution in many separate regions, which are, probably, observed in our Galaxy as infrared bubbles (Churchwell et al. 2006).

A correlation between the F_8/F_{24} ratio and metallicity for our entire sample is presented in Fig. 10a. Metallicity error bars do not include the intrinsic uncertainty of the ONS method which is of the order of 0.08 (Pilyugin, Vílchez & Thuan 2010). For extra clarity points are marked with different colours from blue for low metallicity to red for high metallicity. Having the ‘destructive’ scenario in mind, we may also want to check whether F_8/F_{24} correlates with the $[\text{O III}]\lambda 5007/\text{H}\beta$ ratio, which is the only (albeit poor) UV field hardness parameter that we have at hand. The correlation does exist as Fig. 10b demonstrates but circle colours, showing metallicity, indicate that it may be a mere reflection of the correlation between $[\text{O III}]\lambda 5007/\text{H}\beta$ and $12 + \log(\text{O}/\text{H})$.

Apparently, the correlation between metallicity and the PAH content exists when we consider complexes of all ages. Further, we divided our complexes into five age bins, so that each bin contains about 20 complexes. In Fig. 11 we show correlations between the infrared flux ratio and metallicity for each age bin separately. The corresponding Spearman rank correlation coefficients r_S are indicated on each panel together with the number N of standard deviations by which the sum squared difference of ranks deviates from its value for the null hypothesis (Press et al. 1992). The correlation is strong, with $r_S \sim 0.7 - 0.8$, at all ages. So, contrary to our naïve expectations, the correlation between metallicity and the PAH content (or, at least, the F_8/F_{24} ratio) does not get any stronger with time.

Next we present a correlation between the F_8/F_{24} ratio and age, and here results are even more unexpected. We have divided all our H II complexes into five metallicity groups, again with each group containing about 20 complexes. In

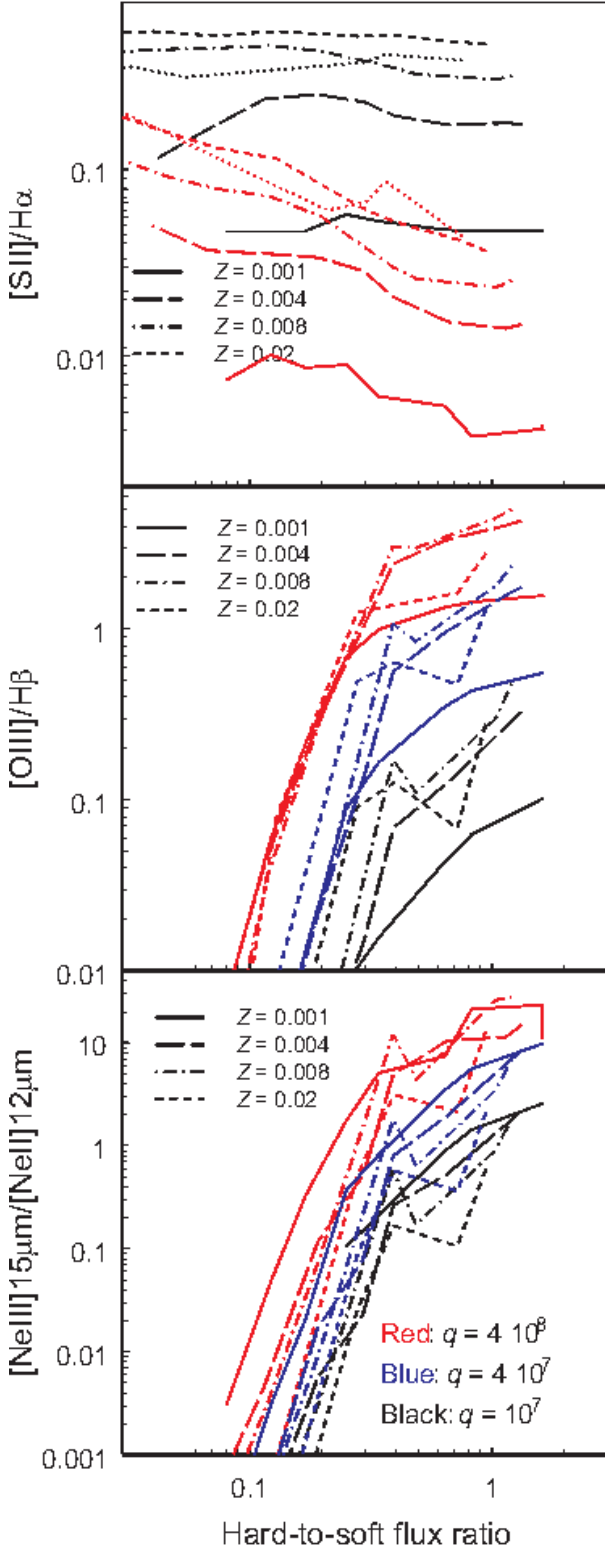


Figure 8. The $[\text{S II}]/\text{H}\alpha$, $[\text{O III}]\lambda 5007/\text{H}\beta$, and $[\text{Ne III}]/[\text{Ne II}]_{12\mu\text{m}}$ line ratios in models with various values of the hard-to-soft flux ratio. Data are taken from the Levesque, Kewley & Larson (2010) model grid. Different linestyles correspond to different metallicity values as indicated in the legends. Line colours on each panel indicate different value of the ionization parameter. Red lines correspond to $q = 4 \times 10^8 \text{ cm s}^{-1}$ (the maximum value in the Levesque et al. grid), blue lines correspond to $q = 4 \times 10^7 \text{ cm s}^{-1}$, black lines correspond to $q = 10^7 \text{ cm s}^{-1}$ (the minimum value in the Levesque et al. grid).

Fig. 12 we plot F_8/F_{24} vs age for all these groups, indicating their metallicity limits, r_S and N . All the complexes are considered, with the one exception.

The correlation for the lowest metallicity bin is not very impressive, with $r_S = 0.42$. However, it is somewhat spoiled by two outliers. One of them is HSK 61 region in Holmberg II (the rightmost point in top left panel of Fig. 12) for which significantly smaller age has been inferred by Stewart et al. (2000) (see Fig. 6). Another outlier is the IC 2574-11 region that has an order of magnitude higher F_8/F_{24} ratio than all the other complexes in this galaxy and is visible as an outlier in Fig. 10 at metallicity of 7.8. This region can be associated with the supernova remnant (Walter et al. (1998), O.V. Egorov et al., 2014). Without these two regions r_S would be 0.51 for this metallicity range.

For a higher metallicity, between 8.0 and 8.3, the correlation coefficient is somewhat higher and it is again positive, corresponding to the F_8/F_{24} ratio growing with age. At even higher metallicity, from 8.3 to 8.45, the correlation becomes almost non-existent. There is again an outlier, NGC 7741-9, the oldest region in our sample. Without it r_S would be somewhat higher, 0.26 instead of 0.09. For $12 + \log(\text{O}/\text{H})$ values between 8.45 and 8.6 the correlation disappears completely.

Finally, for metallicities above 8.6 the correlation arises again, but with the opposite sign. With $r_S = -0.62$, it indicates that the F_8/F_{24} ratio decreases with age. The oldest region in this subsample, +074+064 in NGC 3184, helps to stress the correlation visually, but does not play a defining role. Without this region r_S would be -0.55 in this metallicity range.

Again, contrary to our expectation, the F_8/F_{24} ratio becomes smaller with time only in complexes with high metallicities. At lower metallicities it actually grows. It does not imply, of course, that mass of PAHs in the complex grows, but indicates that particles emitting at $8\mu\text{m}$ become *relatively* more abundant with time than particles emitting at $24\mu\text{m}$.

Our ability to test the connection between the F_8/F_{24} ratio and the hard-to-soft flux ratio is limited as $[\text{O III}]\lambda 5007/\text{H}\beta$ is actually not a good tracer of the radiation field hardness. We have checked whether the F_8/F_{24} ratio correlates with the $[\text{O III}]\lambda 5007/\text{H}\beta$ ratio in separate metallicity bins and found a weak negative correlation in all bins, with r_S of the order of -0.3 . The significance of this correlation is hard to ascertain. Even if $[\text{O III}]\lambda 5007/\text{H}\beta$ were a reliable tracer of the radiation field hardness, it still depends both on age and metallicity. To estimate the role of the radiation hardness directly, we would need to consider groups of H II complexes having similar (preferably low) metallicities *and* ages, provided the radiation hardness within the group varies for some reason, different from metallicity and age. However, our sample is definitely too small for this task.

The summary of our findings is as follows. The mid-infrared flux ratio grows with metallicity at all ages. The negative correlation of the ratio with the $[\text{O III}]\lambda 5007/\text{H}\beta$ mostly reflects the correlation between this ratio and metallicity. When we consider separate metallicity bins, only weak remaining correlation between F_8/F_{24} and $[\text{O III}]\lambda 5007/\text{H}\beta$ is observed. The most interesting result is that the F_8/F_{24} ratio grows with age at low metallicities and decreases with age at high metallicities.

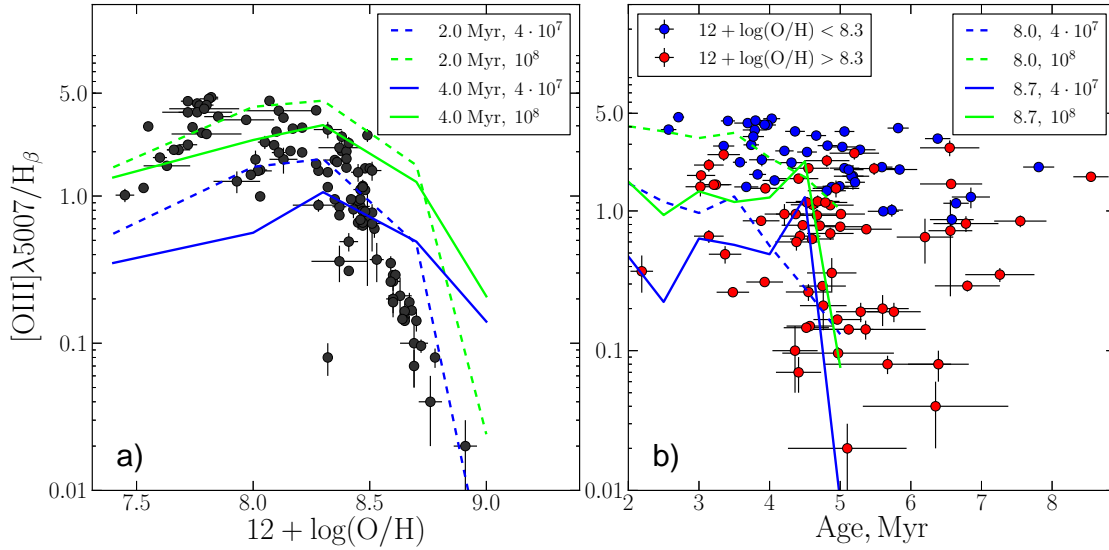


Figure 9. a) Relation between the $[O\ III]\lambda 5007/H\beta$ ratio and the H II complex metallicity. Solid and dashed lines show the relations computed with Levesque, Kewley & Larson (2010) grids for ages of 2 and 4 Myr and ionization parameters of $4 \cdot 10^7$ (blue lines) and 10^8 cm s⁻¹ (green lines). b) Relation between the $[O\ III]\lambda 5007/H\beta$ ratio and age. Regions with metallicity higher than 8.3 are marked by red circles while the rest regions are marked by blue circles. Solid and dashed lines again show relations modelled using Levesque, Kewley & Larson (2010) grids for metallicities 8.0 (dashed lines) and 8.7 (solid lines) and ionization parameters of $4 \cdot 10^7$ (blue lines) and 10^8 cm s⁻¹ (green lines).

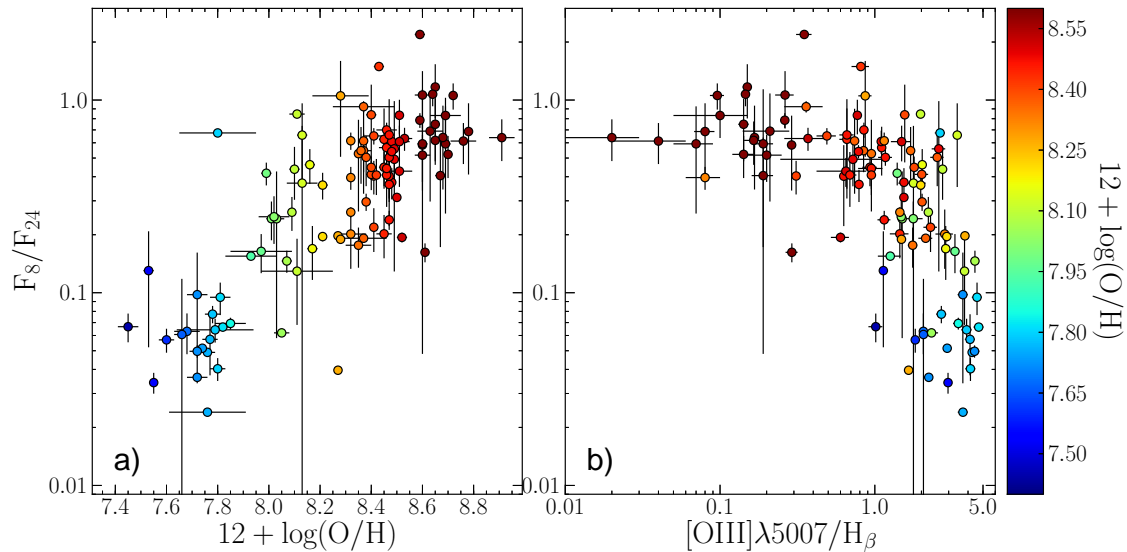


Figure 10. a) The F_8/F_{24} ratio as a function of metallicity in the studied galaxies. Metallicity values are also indicated by colours from blue for low values to violet for high values. b) Relation between the $[O\ III]\lambda 5007/H\beta$ ratio which is often used as an indicator of the radiation field hardness and the infrared flux ratio.

5 DISCUSSION

The main problem we tried to address in this study is the still unexplained origin of the correlation between metallicity and PAH emission (or abundance) shown in Fig. 10 for our sample. This problem was discussed by many authors, and a number of possible explanations were put forward. However, none of these explanations is widely accepted.

One of the hypotheses states that PAHs are more efficiently destroyed in low metallicity environments due to factors intrinsic to such environments. For example, supernova shocks have been invoked as a factor that can rapidly dissociate small particles at low metallicity (O’Halloran, Satyapal & Dudik 2006). However,

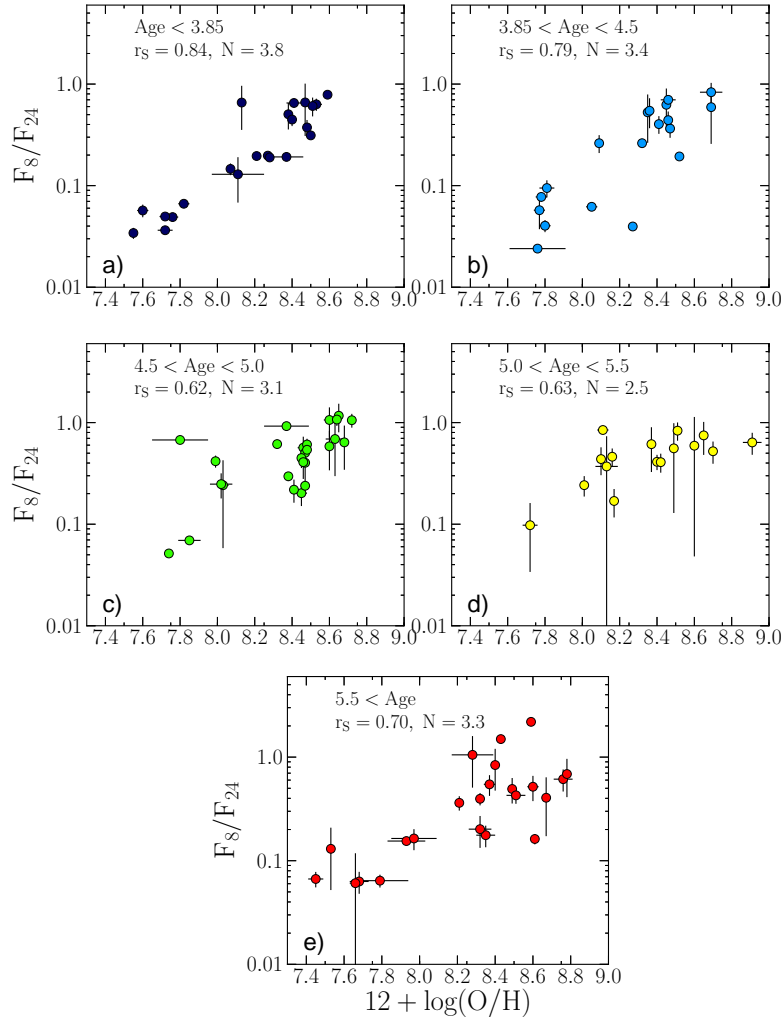


Figure 11. Relation between the infrared flux ratio and the metallicity of the complex for five age bins. Limits for bins are indicated on each panel along with the Spearman rank correlation coefficients r_s and the number N of standard deviations by which the sum squared difference of ranks deviates from its value for the null hypothesis. Various colours are used to denote the H II complex metallicity as indicated by the scale in Fig. 10.

Sandstrom et al. (2010) did not find any correlation between PAHs and supernova shocks in the SMC.

Another plausible destruction factor is the UV field. Using the $[\text{Ne III}]/[\text{Ne II}]$ line ratio as a tracer of the radiation field hardness, Madden (2000) showed that starlight and nebular spectrum is harder in low metallicity medium than in high metallicity medium. In principle, it can be expected that harder UV field, rich in more energetic photons, dissociates PAH particles faster. Khramtsova et al. (2013) presented arguments in favour of the ‘destructive’ scenario of PAH evolution, relating the lower PAH mass fraction in low-metallicity environments to a stronger and/or harder UV field. In this study we approach this problem using an H II complex sample that encompasses a wide metallicity

range. Having estimated ages of the H II complexes, we may try to reveal some evolutionary effects in the PAH content of H II complexes.

Let us first suppose that the only process that regulates the relative PAHs content in H II complexes is their destruction by UV photons. In this case we would expect to see q_{PAH} and the F_8/F_{24} ratio decreasing with age at all metallicities. Also, if the photodestruction efficiency decreases with metallicity, a correlation of the PAH tracers with $12 + \log(\text{O}/\text{H})$ should become stronger with age. None of these predictions is confirmed by our data. The correlation between the F_8/F_{24} ratio and metallicity is already strong in the youngest of our complexes and does not change much with time. The negative correlation of the F_8/F_{24} ratio with

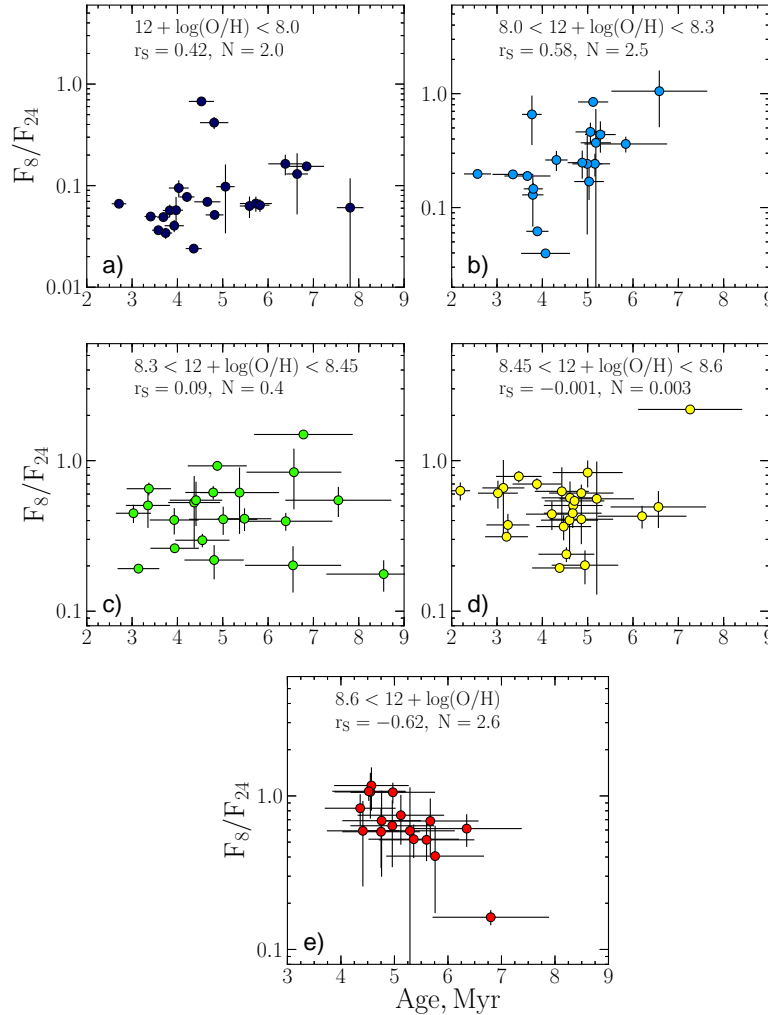


Figure 12. Relation between the infrared flux ratio and the age of the complex for five metallicity bins. Limits for bins are indicated on each panel along with the Spearman rank correlation coefficients. Various colours are used to denote the H II complex metallicity as indicated by the scale in Fig. 10.

age is only seen in the highest metallicity complexes, while in the complexes with low metal content the F_8/F_{24} ratio actually increases with time.

Apparently, the real picture is not limited to just a PAH photodestruction in H II complexes. In particular, the growing F_8/F_{24} ratio does not necessarily mean that q_{PAH} increases. The F_8/F_{24} ratio could also grow in these complexes as a result of more efficient destruction of VSGs (Pilleri et al. 2012). The destruction of larger grains means that the grain size distribution evolves and, strictly speaking, the Draine & Li (2007) model with the size distribution taken from Weingartner & Draine (2001), which we invoked to justify usage of the F_8/F_{24} ratio as a measure of the relative PAH content, may no longer be applicable, and different size distributions should be used. That is, in principle, we

can imagine the situation when F_8/F_{24} is large and q_{PAH} is small.

Then, VSGs may not be simply eliminated. Their destruction can be a gradual process, producing PAHs in its course. If VSGs are indeed precursors of PAHs, the PAH relative abundance and the F_8/F_{24} ratio are determined by a more delicate balance between VSG and PAH photodestruction timescales. For example, if PAHs are more stable to photodestruction than VSGs (Pilleri et al. 2012), their respective abundances would both decrease with time, but abundances of VSGs would drop faster. Also, PAHs formed as a result of VSGs destruction would partially compensate for the destruction of original PAHs.

To explain the observed correlation between the metallicity and the PAH tracers, we might have assumed, for ex-

ample, that the efficiency of VSG destruction is more sensitive to the UV field hardness than the efficiency of PAH destruction. But this assumption has to be reconciled with the lack of correlation between metallicity and the ratio of the $24\ \mu\text{m}$ flux and the flux at longer wavelengths (the P_{24} index introduced in the work of Draine & Li (2007) that was shown in the work of Khramtsova et al. (2013). It implies that VSG destruction occurs irrespective to metallicity and the observed change in the evolution of the F_8/F_{24} ratio from low to high metallicity is related solely to the PAH evolution.

It must be admitted that the original question on the nature of the correlation between the metallicity and the F_8/F_{24} ratio (or q_{PAH}) still remains unanswered. Our data show that the correlation already exists in complexes having ages less than 3 Myr (Fig. 11). So, whatever mechanisms are responsible for this correlation, they are already operative at the early stages of H II complexes evolution or prior to these stages. These mechanisms can be related to the specific details of dust destruction in the youngest H II complexes, or to the details of dust evolution in molecular clouds.

The idea that PAHs and grains of other types can form in molecular clouds is by no means new. Some mechanisms of PAH growth in the dense ISM were suggested as an addition to stellar sources (Greenberg et al. 2000; Parker et al. 2012). There are some observational indications that the PAH abundance increases in dense molecular clouds. Sandstrom et al. (2010) found the correlation between CO and the PAH dust mass fraction in the Small Magellanic Cloud while the correlation of q_{PAH} with the distribution of AGB stars is not observed. They concluded that perhaps those PAHs that we observe in bright H II complexes were formed in cold molecular clouds directly prior to the onset of the star formation, while PAHs ejected by stars were destroyed in the diffuse ISM. If efficiency of PAH formation in molecular clouds depend on metallicity, e.g., through its relation to surface chemistry, we may expect lower PAH content in lower metallicity environment.

To draw more specific conclusions, one would need to consider H II complexes with both optical spectroscopy and far-infrared photometry available. In this study we only use *Spitzer* photometry as it allows considering smaller complexes and complexes in crowded environments. Most of the galaxies from our sample have also been observed with *Herschel* but these data would not help to clarify the situation as they allow studying only large and/or isolated regions. In our sample only H II complexes in Holmberg II correspond to these criteria. Their study is published separately (Wiebe et al. 2014). For other galaxies far infrared and submillimetre data of higher angular resolution are needed, possibly, accessible with the Atacama Large Millimeter Array (ALMA).

6 SUMMARY

Analysis of optical spectroscopy and infrared photometry of H II complexes in nine galaxies is presented. Observational data are used to infer metallicities, ages, and the radiation field hardness in the studied complexes and to estimate the ratio of fluxes at $8\ \mu\text{m}$ and $24\ \mu\text{m}$ considered as an indicator of PAH abundance.

We use the Starburst99 code to compute theoretical spectra for our regions and the grid of theoretical line ratios provided by Levesque, Kewley & Larson (2010) to assess the reliability of [S II]/H α , [O III] λ 5007/H β , and [Ne III] $15\ \mu\text{m}$ /[Ne II] $12\ \mu\text{m}$ line ratios as tracers of the radiation field hardness. This quantity is evaluated as a ratio of integrated fluxes in the ranges from 90\AA to 912\AA and from 912\AA to 2000\AA ('hard-to-soft flux ratio'). The [S II]/H α ratio only depends on the hard-to-soft flux ratio if the ionization parameter, q , is relatively large, $\gtrsim 10^8\ \text{cm s}^{-1}$. At smaller values of q the [S II]/H α ratio does not depend on the hardness of radiation field. Oxygen and neon line ratios are more sensitive to the hard-to-soft flux ratio and can be used as tracers of radiation field hardness, albeit with uncertainty if the ionization parameter is unknown.

Our main conclusions are the following:

- As found in previous studies, the F_8/F_{24} ratio is an increasing function of metallicity in the studied complexes. The [O III] λ 5007/H β line ratio decreases with metallicity, in quantitative agreement with the numerical models. The infrared flux ratio is also correlated with the [O III] λ 5007/H β but the available data are not sufficient to make definitive conclusions about radiation hardness being the driver of the correlation between metallicity and the PAH tracers. In separate metallicity bins the correlation between the F_8/F_{24} ratio and the radiation hardness is much weaker.
- The relative abundance of PAHs (measured with the F_8/F_{24} ratio) grows with age of an H II complex at low metallicities (less than ~ 8.3) and decreases with age in H II complexes with metallicities higher than about 8.6. The correlation between the F_8/F_{24} ratio and metallicity is already present in the youngest complexes from our sample (with ages less than 3 Myr) and does not change appreciably over the following evolution.

The abundance of PAHs in different physical environments is defined by a number of competing processes that can be metallicity-dependent, age-dependent, etc. In order to understand the connection between the PAH abundance and the star formation rate as well as other parameters of star-forming regions, all the processes need to be considered that influence the abundance of PAHs including formation of PAHs in stars, molecular clouds, and H II complexes as well as their destruction by UV photons, shock waves, cosmic rays, shattering etc. All these processes can be equally important in the PAH lifecycle and we still need to find out which of them play the important role and which can be neglected. This study represents yet another step in solving the problem of the PAH evolution and put some additional constraints on various factors that affect this evolution.

ACKNOWLEDGMENTS

We thank the anonymous referee for criticism and suggestions that led to significant improvements of the paper, Kevin Croxall for spectroscopic data on H II complexes in IC 2574 and Emily Levesque for valuable advices. This work was supported by the RFBR grants 12-02-31356, 14-02-31456, 14-02-00604 and also the OFN-17 Research Program of the Division of Physics, Russian Academy of Sciences. This work is based in part on observations obtained with

6-m telescope of the Special Astrophysical Observatory of Russian Academy of Sciences, and in part on observations made with the Spitzer Space Telescope, which is operated by the Jet Propulsion Laboratory, California Institute of Technology under a contract with NASA. We used the HyperLeda database (<http://leda.univ-lyon1.fr>).

REFERENCES

Afanasiev V. L., Moiseev A. V., 2005, *Astronomy Letters*, 31, 194
 Allain T., Leach S., Sedlmayr E., 1996, *A&A*, 305, 602
 Aniano G., Draine B. T., Gordon K. D., Sandstrom K., 2011, *PASP*, 123, 1218
 Asano R. S., Takeuchi T. T., Hirashita H., Nozawa T., 2013, *MNRAS*, 432, 637
 Berné O. et al., 2007, *A&A*, 469, 575
 Bode M. F., Evans A., 2008, *Classical Novae*. Cambridge: Cambridge University Press
 Boersma C., Hony S., Tielens A. G. G. M., 2006, *A&A*, 447, 213
 Bresolin F., Kennicutt, Jr. R. C., Garnett D. R., 1999, *ApJ*, 510, 104
 Cardelli J. A., Clayton G. C., Mathis J. S., 1989, *ApJ*, 345, 245
 Charbonnel C., Meynet G., Maeder A., Schaller G., Schaerer D., 1993, *A&AS*, 101, 415
 Cherchneff I., Barker J. R., Tielens A. G. G. M., 1992, *ApJ*, 401, 269
 Churchwell E. et al., 2006, *ApJ*, 649, 759
 Copetti M. V. F., Pastoriza M. G., Dottori H. A., 1986, *A&A*, 156, 111
 Croxall K. V., van Zee L., Lee H., Skillman E. D., Lee J. C., Côté S., Kennicutt, Jr. R. C., Miller B. W., 2009, *ApJ*, 705, 723
 Dalcanton J. J. et al., 2009, *ApJS*, 183, 67
 Dhanoa H., Rawlings J. M. C., 2014, *MNRAS*, 440, 1786
 Dopita M. A. et al., 2006, *ApJ*, 647, 244
 Draine B. T. et al., 2007, *ApJ*, 663, 866
 Draine B. T., Li A., 2007, *ApJ*, 657, 810
 Draine B. T., Salpeter E. E., 1979, *ApJ*, 231, 77
 Egorov O. V., Lozinskaya T. A., Moiseev A. V., 2013, *MNRAS*, 429, 1450
 Engelbracht C. W., Gordon K. D., Rieke G. H., Werner M. W., Dale D. A., Latter W. B., 2005, *ApJL*, 628, L29
 Epinat B., Amram P., Marcelin M., 2008, *MNRAS*, 390, 466
 Everett J. E., Churchwell E., 2010, *ApJ*, 713, 592
 Fitzpatrick E. L., 1999, *PASP*, 111, 63
 Gail H.-P., Sedlmayr E., 1987, in *NATO ASIC Proc. 210: Physical Processes in Interstellar Clouds*, Morfill G. E., Scholer M., eds., pp. 275–303
 Galliano F., Dwek E., Charnial P., 2008, *ApJ*, 672, 214
 Gordon K. D., Engelbracht C. W., Rieke G. H., Misselt K. A., Smith J.-D. T., Kennicutt, Jr. R. C., 2008, *ApJ*, 682, 336
 Greenberg J. M. et al., 2000, *ApJL*, 531, L71
 Groves B. A., Dopita M. A., Sutherland R. S., 2004, *ApJS*, 153, 9

Gusev A. S., Pilyugin L. S., Sakhibov F., Dodonov S. N., Ezhkova O. V., Khramtsova M. S., 2012, *MNRAS*, 424, 1930
 Gusev A. S., Sakhibov F. H., Dodonov S. N., 2013, *Astrophysical Bulletin*, 68, 40
 Guzman-Ramirez L., Zijlstra A. A., Níchuimín R., Gesicki K., Lagadec E., Millar T. J., Woods P. M., 2011, *MNRAS*, 414, 1667
 Hirashita H., Kobayashi H., 2013, *Earth, Planets, and Space*, 65, 1083
 Hunt L. K., Thuan T. X., Izotov Y. I., Sauvage M., 2010, *ApJ*, 712, 164
 Jacobs B. A., Rizzi L., Tully R. B., Shaya E. J., Makarov D. I., Makarova L., 2009, *AJ*, 138, 332
 Jones A. P., Fanciullo L., Köhler M., Verstraete L., Guillet V., Bocchio M., Ysard N., 2013, *A&A*, 558, A62
 Jones A. P., Nuth J. A., 2011, *A&A*, 530, A44
 Jones A. P., Tielens A. G. G. M., Hollenbach D. J., 1996, *ApJ*, 469, 740
 Jones A. P., Tielens A. G. G. M., Hollenbach D. J., McKee C. F., 1994, *ApJ*, 433, 797
 Karachentsev I. D., Karachentseva V. E., Huchtmeier W. K., Makarov D. I., 2004, *AJ*, 127, 2031
 Kennicutt, Jr. R. C. et al., 2003, *PASP*, 115, 928
 Kewley L. J., Dopita M. A., Sutherland R. S., Heisler C. A., Trevena J., 2001, *ApJ*, 556, 121
 Kewley L. J., Ellison S. L., 2008, *ApJ*, 681, 1183
 Khramtsova M. S., Wiebe D. S., Boley P. A., Pavlyuchenkov Y. N., 2013, *MNRAS*, 431, 2006
 Kobulnicky H. A., Kewley L. J., 2004, *ApJ*, 617, 240
 Latter W. B., 1991, *ApJ*, 377, 187
 Le Page V., Snow T. P., Bierbaum V. M., 2009, *ApJ*, 704, 274
 Lebouteiller V., Bernard-Salas J., Whelan D. G., Brandl B., Galliano F., Charmandaris V., Madden S., Kunth D., 2011, *ApJ*, 728, 45
 Leitherer C. et al., 1999, *ApJS*, 123, 3
 Leonard D. C., Filippenko A. V., Chornock R., Li W., 2002, *AJ*, 124, 2506
 Levesque E. M., Berger E., Kewley L. J., Bagley M. M., 2010, *AJ*, 139, 694
 Levesque E. M., Kewley L. J., Larson K. L., 2010, *AJ*, 139, 712
 Levesque E. M., Richardson M. L. A., 2014, *ApJ*, 780, 100
 Li A., Draine B. T., 2002, *ApJ*, 572, 232
 López-Sánchez Á. R., Dopita M. A., Kewley L. J., Zahid H. J., Nicholls D. C., Scharwächter J., 2012, *MNRAS*, 426, 2630
 Madden S. C., 2000, *New Astronomy Reviews*, 44, 249
 Marble A. R. et al., 2010, *ApJ*, 715, 506
 Matsuura M. et al., 2009, *MNRAS*, 396, 918
 Matsuura M., Woods P. M., Owen P. J., 2013, *MNRAS*, 429, 2527
 Mattiotta A. L., Hudgins D. M., Allamandola L. J., 2005, *ApJ*, 629, 1188
 Meynet G., Maeder A., Schaller G., Schaerer D., Charbonnel C., 1994, *A&AS*, 103, 97
 Micelotta E. R., Jones A. P., Tielens A. G. G. M., 2010a, *A&A*, 510, A37
 Micelotta E. R., Jones A. P., Tielens A. G. G. M., 2010b, *A&A*, 510, A36

- Micelotta E. R., Jones A. P., Tielens A. G. G. M., 2011, *A&A*, 526, A52
- Oey M. S., Kennicutt, Jr. R. C., 1993, *ApJ*, 411, 137
- O’Halloran B., Satyapal S., Dudik R. P., 2006, *ApJ*, 641, 795
- Osterbrock D. E., Ferland G. J., 2006, *Astrophysics of gaseous nebulae and active galactic nuclei*. CA: University Science Books, 2006
- Parker D. S. N., Zhang F., Kim Y. S., Kaiser R. I., Landera A., Kislov V. V., Mebel A. M., Tielens A. G. G. M., 2012, *PNAS*, 109, 53
- Paturel G., Petit C., Prugniel P., Theureau G., Rousseau J., Brouty M., Dubois P., Cambr esy L., 2003, *A&A*, 412, 45
- Peacock M. B., Zepf S. E., Finzell T., 2013, *ApJ*, 769, 126
- Pellerin A., Meyer M. M., Calzetti D., Harris J., 2012, *AJ*, 144, 182
- Pety J., Teyssier D., Foss e D., Gerin M., Roueff E., Abergel A., Habart E., Cernicharo J., 2005, *A&A*, 435, 885
- Pilleri P., Montillaud J., Bern e O., Joblin C., 2012, *A&A*, 542, A69
- Pilyugin L. S., Mattsson L., 2011, *MNRAS*, 412, 1145
- Pilyugin L. S., Thuan T. X., 2005, *ApJ*, 631, 231
- Pilyugin L. S., V lchez J. M., Thuan T. X., 2010, *ApJ*, 720, 1738
- Press W. H., Teukolsky S. A., Vetterling W. T., Flannery B. P., 1992, *Numerical recipes in FORTRAN. The art of scientific computing*. Cambridge: University Press, —c1992, 2nd ed.
- Robitaille T. P., Churchwell E., Benjamin R. A., Whitney B. A., Wood K., Babler B. L., Meade M. R., 2012, *A&A*, 545, A39
- Ryder S. D., 1995, *ApJ*, 444, 610
- Ryter C., 1991, *Annales de Physique*, 16, 507
- Saintonge A., Giovanelli R., Haynes M. P., Hoffman G. L., Kent B. R., Martin A. M., Stierwalt S., Brosch N., 2008, *AJ*, 135, 588
- Salonen E., 2002, PhD Thesis, Helsinki University
- Sandstrom K. M., Bolatto A. D., Draine B. T., Bot C., Stanimirovi c S., 2010, *ApJ*, 715, 701
- Schaerer D., Charbonnel C., Meynet G., Maeder A., Schaller G., 1993a, *A&AS*, 102, 339
- Schaerer D., Meynet G., Maeder A., Schaller G., 1993b, *A&AS*, 98, 523
- Schaerer D., Vacca W. D., 1998, *ApJ*, 497, 618
- Schaller G., Schaerer D., Meynet G., Maeder A., 1992, *A&AS*, 96, 269
- Slater C. T. et al., 2011, *ApJ*, 732, 98
- Smith J. D. T. et al., 2007, *ApJ*, 656, 770
- Stasi nska G., 2004, in *Cosmochemistry. The melting pot of the elements*, Esteban C., Garc a L pez R., Herrero A., S nchez F., eds., pp. 115–170
- Stasi nska G., Leitherer C., 1996, *ApJS*, 107, 661
- Stewart S. G. et al., 2000, *ApJ*, 529, 201
- Stewart S. G., Walter F., 2000, *AJ*, 120, 1794
- Sutherland R. S., Dopita M. A., 1993, *ApJS*, 88, 253
- Tully R. B., Rizzi L., Shaya E. J., Courtois H. M., Makarov D. I., Jacobs B. A., 2009, *AJ*, 138, 323
- van Zee L., Salzer J. J., Haynes M. P., O’Donoghue A. A., Balonek T. J., 1998, *AJ*, 116, 2805
- Vila-Costas M. B., Edmunds M. G., 1992, *MNRAS*, 259, 121
- Vilchez J. M., Pagel B. E. J., 1988, *MNRAS*, 231, 257
- Walter F., Kerp J., Duric N., Brinks E., Klein U., 1998, *ApJL*, 502, L143
- Weingartner J. C., Draine B. T., 2001, *ApJ*, 548, 296
- Wiebe D. S., Egorov O. V., Lozinskaya T. A., 2011, *Astronomy Reports*, 55, 585
- Wiebe D. S., Khramtsova M. S., Egorov O. V., Lozinskaya T. A., 2014, *Astronomy Letters*, 40, 278–290
- Willick J. A., Courteau S., Faber S. M., Burstein D., Dekel A., Strauss M. A., 1997, *ApJS*, 109, 333
- Woods P. M., Willacy K., 2007, *ApJL*, 655, L49
- Wu H., Zhu Y.-N., Cao C., Qin B., 2007, *ApJ*, 668, 87
- Zaritsky D., Kennicutt, Jr. R. C., Huchra J. P., 1994, *ApJ*, 420, 87

Table 2: List of studied H II complexes in galaxies IC 1727 and NGC 7741 and results of spectroscopy of H II complexes. The table contains designations of complexes, equatorial coordinates, bright line intensities in studied H II complexes normalised to H β , equivalent width of the H β line, metallicity estimated by the ‘ONS’ method and radial distance from the centre of a galaxy normalised to a R $_{25}$.

Complex	α offset ''	δ offset ''	I([O II]) $\lambda 3727 + \lambda 3729$	I([O III]) $\lambda 4959$	I([O III]) $\lambda 5007$	I(H α)	I([N II]) $\lambda 6548 + \lambda 6584$	I([S II]) $\lambda 6717 + \lambda 6731$	EW(H β) Å	E(B-V)	12 + log(O/H) ONS	r/R_{25}
IC 1727												
IC 1727-1	+1.68	-29.5	2.57 \pm 0.67	0.63 \pm 0.08	1.88 \pm 0.06	3.07 \pm 0.15	0.41 \pm 0.17	1.14 \pm 0.18	103.9 \pm 0.6	0.33 \pm 0.03	8.07 \pm 0.03	0.19
IC 1727-2	+1.61	-25.0	2.85 \pm 0.23	1.02 \pm 0.03	3.13 \pm 0.03	2.85 \pm 0.05	0.18 \pm 0.07	0.47 \pm 0.09	91.8 \pm 0.4	0.29 \pm 0.03	8.02 \pm 0.04	0.18
IC 1727-3	+1.23	-18.9	2.85 \pm 0.23	1.02 \pm 0.03	3.13 \pm 0.03	2.85 \pm 0.05	0.18 \pm 0.07	0.47 \pm 0.09	44.9 \pm 0.1	0.33 \pm 0.02	8.04 \pm 0.06	0.14
IC 1727-4	+1.10	-16.5	3.87 \pm 0.31	0.50 \pm 0.03	1.51 \pm 0.03	2.85 \pm 0.07	0.32 \pm 0.10	0.69 \pm 0.09	51.1 \pm 0.3	0.22 \pm 0.02	8.03 \pm 0.04	0.12
IC 1727-5	+0.59	-5.0	3.86 \pm 0.18	0.51 \pm 0.02	1.53 \pm 0.03	2.87 \pm 0.05	0.33 \pm 0.07	0.71 \pm 0.05	52.7 \pm 0.3	0.24 \pm 0.02	8.04 \pm 0.03	0.41
IC 1727-6	+2.17	-29.3	3.59 \pm 0.20	0.52 \pm 0.02	1.47 \pm 0.03	2.92 \pm 0.06	0.26 \pm 0.11	0.90 \pm 0.07	60.2 \pm 0.5	0.33 \pm 0.04	8.05 \pm 0.05	0.26
IC 1727-7	+1.95	-26.2	4.22 \pm 0.25	0.45 \pm 0.02	1.38 \pm 0.03	2.72 \pm 0.05	0.26 \pm 0.06	0.78 \pm 0.06	25.1 \pm 0.1	0.36 \pm 0.04	8.04 \pm 0.04	0.24
IC 1727-8	+1.77	-17.5	2.34 \pm 0.11	1.43 \pm 0.01	4.20 \pm 0.01	2.88 \pm 0.02	0.17 \pm 0.02	0.52 \pm 0.03	55.4 \pm 0.1	0.34 \pm 0.15	8.07 \pm 0.03	0.22
IC 1727-9	+0.56	+13.65	4.44 \pm 0.66	0.41 \pm 0.06	1.09 \pm 0.07	3.02 \pm 0.10	0.24 \pm 0.14	0.82 \pm 0.37	22.1 \pm 1.1	0.32 \pm 0.05	7.94 \pm 0.09	0.13
IC 1727-10	-5.92	+81.4	5.18 \pm 0.39	0.72 \pm 0.03	2.12 \pm 0.04	2.88 \pm 0.03	0.23 \pm 0.04	0.46 \pm 0.07	120.0 \pm 1.1	0.06 \pm 0.03	8.05 \pm 0.04	0.69
IC 1727-11	-6.49	+110.0	2.57 \pm 1.12	1.24 \pm 0.11	3.86 \pm 0.11	2.86 \pm 0.13	0.28 \pm 0.22	0.56 \pm 0.30	129.3 \pm 2.5	0.06 \pm 0.03	8.00 \pm 0.03	0.79
NGC 7741												
NGC 7741-1	+3.45	+1.8	2.44 \pm 0.72	0.59 \pm 0.07	1.79 \pm 0.06	2.93 \pm 0.07	0.61 \pm 0.09	1.12 \pm 0.11	44.8 \pm 0.8	0.23 \pm 0.05	8.13 \pm 0.13	0.62
NGC 7741-2	+0.68	+1.6	3.69 \pm 0.82	0.39 \pm 0.08	1.12 \pm 0.09	2.78 \pm 0.12	0.77 \pm 0.14	1.12 \pm 0.24	4.8 \pm 0.2	0.34 \pm 0.19	8.47 \pm 0.04	0.12
NGC 7741-3	-0.72	+5.4	2.72 \pm 0.14	0.19 \pm 0.03	0.62 \pm 0.02	2.79 \pm 0.03	0.82 \pm 0.05	0.81 \pm 0.05	13.7 \pm 0.2	0.34 \pm 0.03	8.47 \pm 0.11	0.13
NGC 7741-4	-1.29	+5.4	3.48 \pm 0.26	0.20 \pm 0.03	0.71 \pm 0.03	2.84 \pm 0.03	0.67 \pm 0.05	0.71 \pm 0.07	8.6 \pm 0.1	0.39 \pm 0.06	8.39 \pm 0.06	0.23
NGC 7741-5	-1.61	+5.4	2.35 \pm 0.25	0.28 \pm 0.04	0.88 \pm 0.04	2.87 \pm 0.05	0.71 \pm 0.08	0.66 \pm 0.13	18.7 \pm 0.2	0.18 \pm 0.03	8.44 \pm 0.05	0.28
NGC 7741-6	-1.90	+5.9	4.43 \pm 0.88	0.36 \pm 0.08	1.04 \pm 0.10	2.82 \pm 0.14	0.58 \pm 0.19	0.94 \pm 0.24	12.1 \pm 0.4	0.20 \pm 0.07	8.30 \pm 0.05	0.34
NGC 7741-7	-3.76	+10.7	3.21 \pm 1.14	0.25 \pm 0.09	0.80 \pm 0.09	2.84 \pm 0.10	0.50 \pm 0.13	0.73 \pm 0.37	13.5 \pm 0.4	0.26 \pm 0.09	8.29 \pm 0.06	0.66
NGC 7741-8	+2.18	-0.8	2.69 \pm 0.60	0.56 \pm 0.06	1.60 \pm 0.06	2.87 \pm 0.06	0.48 \pm 0.09	0.68 \pm 0.23	47.0 \pm 1.0	0.04 \pm 0.03	8.33 \pm 0.04	0.40
NGC 7741-9	+1.93	+11.7	2.24 \pm 0.26	0.64 \pm 0.02	1.77 \pm 0.02	2.85 \pm 0.03	0.47 \pm 0.06	0.50 \pm 0.10	5.5 \pm 0.1	0.13 \pm 0.03	8.35 \pm 0.03	0.39
NGC 7741-10	+1.78	+19.9	2.27 \pm 0.32	0.94 \pm 0.01	2.81 \pm 0.01	2.84 \pm 0.04	0.38 \pm 0.05	0.42 \pm 0.12	13.3 \pm 0.1	0.07 \pm 0.01	8.30 \pm 0.03	0.42

Table 3: Results of aperture infrared photometry of H II complexes including designation of a complex, equatorial coordinates, aperture size, and fluxes at 3.6, 4.5, 5.8, 8.0 and 24 μ m.

Complex	α (J2000)			δ (J2000)			Aperture radius, ''	$F_{3.6}$, mJy	$F_{4.5}$, mJy	$F_{5.8}$, mJy	$F_{8.0}$, mJy	$F_{8.0}^{ale}$, mJy	F_{24} , mJy	F_{24}^{HS} , mJy
	h	m	s	o	'	''								
IC 1727														
IC 1727-3	01 47 31.14	+27 19 38.39	8.0	0.237 \pm 0.032	0.241 \pm 0.032	0.516 \pm 0.051	0.782 \pm 0.097	0.488 \pm 0.094	2.100 \pm 0.242	2.013 \pm 0.242				
IC 1727-5	01 47 30.44	+27 19 52.51	8.0	0.152 \pm 0.026	0.154 \pm 0.027	0.155 \pm 0.041	0.216 \pm 0.061	0.095 \pm 0.060	0.448 \pm 0.163	0.392 \pm 0.163				
IC 1727-6	01 47 32.09	+27 19 28.72	8.0	0.141 \pm 0.033	0.144 \pm 0.033	0.346 \pm 0.060	0.627 \pm 0.102	0.426 \pm 0.098	1.770 \pm 0.263	1.718 \pm 0.263				
IC 1727-9	01 47 30.46	+27 19 11.38	8.0	0.084 \pm 0.035	0.086 \pm 0.035	0.199 \pm 0.046	0.131 \pm 0.054	0.042 \pm 0.055	0.303 \pm 0.095	0.272 \pm 0.096				
IC 1727-10	01 47 24.00	+27 19 19.00	8.0	0.011 \pm 0.011	0.011 \pm 0.011	0.002 \pm 0.018	0.024 \pm 0.023	0.017 \pm 0.024	0.279 \pm 0.056	0.0275 \pm 0.056				
IC 1727-11	01 47 23.41	+27 19 49.98	8.0	0.016 \pm 0.008	0.016 \pm 0.008	0.040 \pm 0.013	0.069 \pm 0.022	0.048 \pm 0.022	0.379 \pm 0.059	0.373 \pm 0.059				
NGC 7741														
NGC 7741-1	23 43 58.462	+26 04 21.95	6.0	0.0134 \pm 0.027	0.007 \pm 0.017	0.043 \pm 0.046	0.133 \pm 0.103	0.107 \pm 0.097	0.290 \pm 0.108	0.290 \pm 0.108				
NGC 7741-3	23 43 54.343	+26 04 34.94	6.0	0.958 \pm 0.204	0.664 \pm 0.138	2.240 \pm 0.403	5.070 \pm 0.878	3.754 \pm 0.843	7.640 \pm 1.220	7.623 \pm 1.220				
NGC 7741-4	23 43 53.695	+26 04 33.21	6.0	1.530 \pm 0.202	1.050 \pm 0.140	3.560 \pm 0.442	7.980 \pm 1.050	5.826 \pm 1.015	10.700 \pm 1.540	10.670 \pm 1.540				
NGC 7741-7	23 43 52.301	+26 04 29.74	6.0	0.235 \pm 0.083	0.154 \pm 0.055	0.739 \pm 0.186	1.850 \pm 0.440	1.247 \pm 0.456	1.190 \pm 0.434	1.186 \pm 0.434				
NGC 7741-9	23 43 56.877	+26 04 39.74	6.0	0.222 \pm 0.058	0.227 \pm 0.043	0.791 \pm 0.144	1.810 \pm 0.312	1.426 \pm 0.294	8.090 \pm 0.919	8.086 \pm 0.919				
NGC 7741-10	23 43 56.719	+26 04 47.64	6.0	0.111 \pm 0.052	0.103 \pm 0.043	0.592 \pm 0.132	1.330 \pm 0.283	1.052 \pm 0.267	5.220 \pm 1.180	5.218 \pm 1.180				
Holmberg II														
HSK 7	08 18 49.80	+70 44 48.92	10.0	0.225 \pm 0.008	0.277 \pm 0.007	0.472 \pm 0.008	0.773 \pm 0.014	0.503 \pm 0.014	10.200 \pm 0.118	10.118 \pm 0.118				
HSK 15	08 18 54.92	+70 43 11.34	8.0	0.142 \pm 0.019	0.097 \pm 0.014	0.097 \pm 0.017	0.075 \pm 0.016	0.001 \pm 0.017	0.781 \pm 0.077	0.730 \pm 0.078				
HSK 16-17	08 18 54.92	+70 42 57.95	8.0	0.083 \pm 0.026	0.079 \pm 0.019	0.118 \pm 0.012	0.156 \pm 0.015	0.086 \pm 0.019	1.350 \pm 0.052	1.320 \pm 0.053				
HSK 20	08 18 56.27	+70 42 38.27	10.0	0.061 \pm 0.010	0.036 \pm 0.008	0.107 \pm 0.009	0.118 \pm 0.009	0.066 \pm 0.010	0.989 \pm 0.070	0.967 \pm 0.070				
HSK 25	08 18 59.90	+70 43 01.02	6.0	0.029 \pm 0.019	0.018 \pm 0.015	0.056 \pm 0.013	0.073 \pm 0.024	0.045 \pm 0.025	0.353 \pm 0.074	0.343 \pm 0.075				
HSK 31	08 19 02.66	+70 42 59.41	10.0	0.007 \pm 0.014	0.004 \pm 0.010	0.059 \pm 0.021	0.066 \pm 0.021	0.046 \pm 0.021	0.474 \pm 0.069	0.471 \pm 0.070				
HSK 59	08 19 23.66	+70 42 58.95	8.0	0.001 \pm 0.010	0.005 \pm 0.007	0.023 \pm 0.005	0.107 \pm 0.011	0.091 \pm 0.011	1.590 \pm 0.096	1.590 \pm 0.096				
HSK 61	08 19 23.13	+70 41 54.07	10.0	0.053 \pm 0.010	0.051 \pm 0.009	0.053 \pm 0.016	0.051 \pm 0.010	0.014 \pm 0.011	0.231 \pm 0.071	0.212 \pm 0.071				
HSK 67	08 19 26.70	+70 41 55.40	10.0	0.100 \pm 0.007	0.110 \pm 0.006	0.144 \pm 0.011	0.177 \pm 0.009	0.090 \pm 0.009	2.570 \pm 0.156	2.534 \pm 0.156				
HSK 70	08 19 27.69	+70 42 20.62	8.0	0.126 \pm 0.148	0.125 \pm 0.116	0.072 \pm 0.099	0.156 \pm 0.049	0.076 \pm 0.086	1.460 \pm 0.095	1.414 \pm 0.109				
HSK 71-73	08 19 28.98	+70 43 01.00	10.0	0.253 \pm 0.012	0.386 \pm 0.013	0.846 \pm 0.021	1.370 \pm 0.025	0.932 \pm 0.025	25.500 \pm 0.378	25.408 \pm 0.378				
HSK 45	08 19 12.69	+70 43 07.44	11.0	0.630 \pm 0.213	1.940 \pm 0.107	4.800 \pm 0.123	7.060 \pm 0.140	4.828 \pm 0.164	25.300 \pm 0.345	25.072 \pm 0.354				
IC 2574														
IC 2574-1	10 28 55.571	+68 27 54.7	8.0	0.019 \pm 0.006	0.015 \pm 0.006	0.063 \pm 0.011	0.136 \pm 0.007	0.105 \pm 0.007	2.120 \pm 0.045	2.117 \pm 0.045				
IC 2574-2	10 28 58.93	+68 28 27.72	7.0	0.044 \pm 0.004	0.045 \pm 0.004	0.080 \pm 0.007	0.151 \pm 0.010	0.109 \pm 0.009	1.410 \pm 0.077	1.402 \pm 0.077				
IC 2574-3	10 28 48.35	+68 28 03.14	9.0	0.301 \pm 0.027	0.333 \pm 0.018	0.970 \pm 0.043	2.140 \pm 0.079	1.648 \pm 0.075	24.900 \pm 0.529	24.850 \pm 0.529				
IC 2574-5	10 28 50.11	+68 28 23.64	8.0	0.087 \pm 0.020	0.080 \pm 0.019	0.202 \pm 0.024	0.384 \pm 0.040	0.285 \pm 0.038	3.020 \pm 0.409	3.005 \pm 0.409				
IC 2574-6	10 28 48.82	+68 28 34.96	7.0	0.054 \pm 0.015	0.059 \pm 0.015	0.087 \pm 0.021	0.162 \pm 0.035	0.113 \pm 0.036	1.990 \pm 0.271	1.980 \pm 0.271				
IC 2574-8	10 28 43.57	+68 28 25.79	8.0	0.170 \pm 0.022	0.215 \pm 0.025	0.261 \pm 0.025	0.405 \pm 0.035	0.260 \pm 0.033	6.480 \pm 0.280	6.450 \pm 0.280				
IC 2574-9	10 28 37.25	+68 28 00.71	8.0	0.089 \pm 0.008	0.076 \pm 0.007	0.110 \pm 0.009	0.213 \pm 0.009	0.149 \pm 0.009	2.170 \pm 0.076	2.154 \pm 0.076				
IC 2574-10	10 28 38.99	+68 28 05.31	6.0	0.052 \pm 0.011	0.047 \pm 0.009	0.055 \pm 0.011	0.050 \pm 0.009	0.022 \pm 0.009	0.239 \pm 0.113	0.229 \pm 0.113				
IC 2574-11	10 28 39.97	+68 28 31.01	8.0	0.008 \pm 0.009	0.008 \pm 0.008	0.011 \pm 0.007	0.051 \pm 0.008	0.039 \pm 0.012	0.059 \pm 0.093	0.058 \pm 0.093				
IC 2574-13	10 28 32.53	+68 28 01.15	8.0	0.014 \pm 0.009	0.006 \pm 0.006	0.010 \pm 0.007	0.008 \pm 0.001	0.003 \pm 0.001	0.116 \pm 0.041	0.114 \pm 0.041				
IC 2574-14	10 28 30.71	+68 28 08.27	7.0	0.031 \pm 0.009	0.026 \pm 0.007	0.053 \pm 0.004	0.064 \pm 0.005	0.040 \pm 0.005	0.631 \pm 0.033	0.625 \pm 0.033				
NGC 628														
NGC 628-7	1 36 47.257	+15 45 50.21	10.0	0.620 \pm 0.048	0.518 \pm 0.037	3.190 \pm 0.212	8.370 \pm 0.524	6.207 \pm 0.504	9.630 \pm 0.517	9.531 \pm 0.517				
NGC 628-8	1 36 51.220	+15 45 58.80	6.0	0.091 \pm 0.029	0.080 \pm 0.024	0.655 \pm 0.173	1.640 \pm 0.427	1.217 \pm 0.412	1.960 \pm 0.563	1.946 \pm 0.563				
NGC 628-10	1 36 53.931	+15 46 56.26	12.0	0.397 \pm 0.025	0.277 \pm 0.019	2.790 \pm 0.116	6.650 \pm 0.246	4.597 \pm 0.245	5.040 \pm 0.205	4.977 \pm 0.205				
+081-140	1 36 47.257	+15 44 44.24	10.0	0.209 \pm 0.025	0.164 \pm 0.017	0.670 \pm 0.128	1.590 \pm 0.313	1.159 \pm 0.299	2.080 \pm 0.242	2.047 \pm 0.242				
+062-158	1 36 45.877	+15 44 24.55	11.0	0.118 \pm 0.030	0.101 \pm 0.020	0.901 \pm 0.165	2.460 \pm 0.448	1.711 \pm 0.445	1.630 \pm 0.328	1.611 \pm 0.328				
+047-172	1 36 44.747	+15 44 05.46	14.0	0.155 \pm 0.037	0.128 \pm 0.026	1.140 \pm 0.180	3.230 \pm 0.443	2.371 \pm 0.428	2.870 \pm 0.269	2.845 \pm 0.269				
+044-175	1 36 43.908	+15 43 49.04	12.0	0.081 \pm 0.020	0.077 \pm 0.015	0.497 \pm 0.067	1.170 \pm 0.158	0.897 \pm 0.150	2.410 \pm 0.186	2.397 \pm 0.186				
+178-052	1 36 53.945	+15 46 10.63	12.0	0.145 \pm 0.014	0.120 \pm 0.010	1.450 \pm 0.083	2.690 \pm 0.119	1.823 \pm 0.121	2.630 \pm 0.161	2.607 \pm 0.161				
-086+186	1 36 35.643	+15 50 07.64	11.0	0.433 \pm 0.023	0.378 \pm 0.016	2.480 \pm 0.076	6.160 \pm 0.192	4.820 \pm 0.182	15.500 \pm 0.396	15.431 \pm 0.396				
-075+200	1 36 36.803	+15 50 27.46	11.0	0.305 \pm 0.020	0.233 \pm 0.017	1.700 \pm 0.109	4.600 \pm 0.300	3.473 \pm 0.292	5.750 \pm 0.627	5.701 \pm 0.627				
NGC 925														
+042-011	2 27 19.989	+33 34 35.21	6.0	0.345 \pm 0.053	0.301 \pm 0.039	1.790 \pm 0.246	4.540 \pm 0.668	3.467 \pm 0.633	8.600 \pm 0.921	8.499 \pm 0.921				
+135-016	2 27 27.607	+33 34 28.03	5.0	0.083 \pm 0.019	0.063 \pm 0.013	0.313 \pm 0.049	0.740 \pm 0.100	0.547 \pm 0.095	1.210 \pm 0.129	1.186 \pm 0.129				
+087-031	2 27 22.709	+33 34 15.91	5.0	0.041 \pm 0.015	0.030 \pm 0.010	0.209 \pm 0.051	0.558 \pm 0.133	0.422 \pm 0.127	0.784 \pm 0.100	0.772 \pm 0.100				
-012-066	2 27 15.893	+33 33 37.92	10.0	0.256 \pm 0.025	0.242 \pm 0.018	1.370 \pm 0.072	3.370 \pm 0.133	2.650 \pm 0.126	13.500 \pm 0.245	13.425 \pm 0.245				
-047-058	2 27 13.206	+33 33 47.48	8.0	0.082 \pm 0.008	0.065 \pm 0.005	0.384 \pm 0.018	0.927 \pm 0.058	0.674 \pm 0.056	1.120 \pm 0.067	1.096 \pm 0.067				
-137+056	2 27 08.015	+33 35 46.95	7.0	0.073 \pm 0.010	0.060 \pm 0.008	0.238 \pm 0.018	0.600 \pm 0.045	0.447 \pm 0.043	1.020 \pm 0.098	0.999 \pm 0.098				
-080+087	2 27 10.526	+33 36 11.28	8.0	0.232 \pm 0.017	0.205 \pm 0.013	1.180 \pm 0.053	2.900 \pm 0.133	2.257 \pm 0.125	8.690 \pm 0.224	8.622 \pm 0.224				
-114+087	2 27 07.676	+33 36 13.08	6.0	0.125 \pm 0.016	0.098 \pm 0.013	0.380 \pm 0.044	0.880 \pm 0.094	0.653 \pm 0.090	1.840 \pm 0.142	1.804 \pm 0.142				
-198-013	2 27 01.378	+33 34 37.25	5.0	0.075 \pm 0.018	0.067 \pm 0.017	0.457 \pm 0.087	1.150 \pm 0.214	0.840 \pm 0.						

Table 3: Results of aperture infrared photometry of H II complexes including designation of a complex, equatorial coordinates, aperture size, and fluxes at 3.6, 4.5, 5.8, 8.0 and 24 μ m.

Complex	α (J2000)			δ (J2000)			Aperture radius, ''	$F_{3.6}$, mJy	$F_{4.5}$, mJy	$F_{5.8}$, mJy	$F_{8.0}$, mJy	$F_{8.0}^{\text{aie}}$, mJy	F_{24} , mJy	F_{24}^{HS} , mJy
	h	m	s	o	'	''								
+059-079	10 18 22.229	+41 24 10.52	7.0	0.084 \pm 0.023	0.069 \pm 0.016	0.421 \pm 0.092	1.100 \pm 0.272	0.792 \pm 0.260	1.090 \pm 0.148	1.058 \pm 0.148				
+092-093	10 18 25.090	+41 23 55.02	6.0	0.092 \pm 0.011	0.074 \pm 0.008	0.513 \pm 0.036	1.400 \pm 0.097	0.965 \pm 0.096	0.936 \pm 0.081	0.901 \pm 0.081				
+111-102	10 18 26.540	+41 23 43.98	8.0	0.018 \pm 0.011	0.009 \pm 0.008	0.028 \pm 0.030	0.073 \pm 0.067	0.047 \pm 0.067	0.038 \pm 0.048	0.031 \pm 0.048				
+005+135	10 18 17.283	+41 27 42.55	8.0	0.223 \pm 0.020	0.170 \pm 0.013	1.320 \pm 0.069	3.200 \pm 0.179	2.369 \pm 0.171	4.470 \pm 0.147	4.385 \pm 0.147				
-017+137	10 18 15.430	+41 27 43.59	8.0	0.116 \pm 0.016	0.098 \pm 0.010	0.749 \pm 0.046	1.890 \pm 0.105	1.348 \pm 0.102	1.760 \pm 0.076	1.716 \pm 0.076				
NGC 3621														
s5a2	11 18 20.861	-32 48 51.97	7.0	0.162 \pm 0.087	0.155 \pm 0.061	1.300 \pm 0.293	3.540 \pm 0.755	2.864 \pm 0.710	14.200 \pm 0.743	14.173 \pm 0.743				
s5a1	11 18 18.838	-32 47 42.59	9.0	1.280 \pm 0.113	1.260 \pm 0.078	7.660 \pm 0.370	18.700 \pm 0.881	14.855 \pm 0.829	76.900 \pm 1.190	76.689 \pm 1.190				
p1a8	11 18 13.589	-32 47 28.51	9.0	0.781 \pm 0.180	0.703 \pm 0.132	5.660 \pm 0.749	14.900 \pm 1.910	11.572 \pm 1.809	27.200 \pm 1.900	27.071 \pm 1.900				
p2a6	11 18 14.707	-32 48 24.56	6.0	0.163 \pm 0.194	0.131 \pm 0.125	0.880 \pm 0.385	2.480 \pm 0.964	1.857 \pm 0.926	2.720 \pm 0.736	2.693 \pm 0.737				
p1a9	11 18 08.489	-32 47 43.11	5.0	0.037 \pm 0.036	0.029 \pm 0.024	0.004 \pm 0.049	0.050 \pm 0.092	0.037 \pm 0.089	0.200 \pm 0.065	0.194 \pm 0.065				
p2a7	11 18 10.550	-32 48 00.63	7.0	0.027 \pm 0.036	0.023 \pm 0.025	1.420 \pm 0.094	3.590 \pm 0.251	2.774 \pm 0.239	5.510 \pm 0.224	5.506 \pm 0.224				
p1a7	11 18 12.094	-32 48 23.85	7.0	0.064 \pm 0.098	0.074 \pm 0.067	0.898 \pm 0.314	2.500 \pm 0.813	1.891 \pm 0.783	2.880 \pm 0.960	2.869 \pm 0.960				
p1a6	11 18 18.638	-32 48 15.25	7.0	0.742 \pm 0.198	0.653 \pm 0.132	5.530 \pm 0.533	14.000 \pm 1.330	10.403 \pm 1.274	16.600 \pm 0.999	16.478 \pm 1.000				
p2a5	11 18 13.507	-32 49 08.33	5.0	0.118 \pm 0.082	0.107 \pm 0.055	0.799 \pm 0.143	2.170 \pm 0.327	1.572 \pm 0.319	1.910 \pm 0.226	1.891 \pm 0.226				
p1a5	11 18 18.178	-32 48 55.75	7.0	1.090 \pm 0.309	0.872 \pm 0.200	5.760 \pm 0.856	15.600 \pm 2.380	11.691 \pm 2.284	18.500 \pm 2.690	18.320 \pm 2.690				
p2a4	11 18 18.929	-32 49 10.57	7.0	0.877 \pm 0.245	0.711 \pm 0.163	5.310 \pm 1.020	14.000 \pm 2.740	10.691 \pm 2.604	20.800 \pm 2.570	20.655 \pm 2.570				
p1a3	11 18 18.830	-32 50 16.04	8.0	0.342 \pm 0.085	0.255 \pm 0.058	1.820 \pm 0.274	4.670 \pm 0.718	3.488 \pm 0.685	5.790 \pm 0.430	5.734 \pm 0.430				
s1a4	11 18 22.207	-32 51 40.22	5.0	0.024 \pm 0.071	0.025 \pm 0.056	0.331 \pm 0.267	0.963 \pm 0.195	0.754 \pm 0.202	1.500 \pm 0.173	1.496 \pm 0.173				
p2a2	11 18 21.480	-32 50 05.82	5.0	0.127 \pm 0.027	0.095 \pm 0.019	0.958 \pm 0.135	2.470 \pm 0.358	1.912 \pm 0.339	4.290 \pm 0.416	4.269 \pm 0.416				
s2a2	11 18 21.842	-32 49 54.36	6.0	0.159 \pm 0.046	0.152 \pm 0.032	0.804 \pm 0.177	2.030 \pm 0.449	1.557 \pm 0.426	3.840 \pm 0.609	3.814 \pm 0.609				
p2a1	11 18 25.442	-32 50 26.44	5.0	0.021 \pm 0.007	0.017 \pm 0.004	0.154 \pm 0.022	0.318 \pm 0.042	0.236 \pm 0.041	0.538 \pm 0.070	0.535 \pm 0.070				
p1a2	11 18 23.815	-32 50 04.60	5.0	0.134 \pm 0.014	0.113 \pm 0.010	0.442 \pm 0.049	1.010 \pm 0.123	0.752 \pm 0.117	1.850 \pm 0.133	1.828 \pm 0.133				
s2a3	11 18 18.765	-32 49 24.59	6.0	0.515 \pm 0.222	0.398 \pm 0.171	2.160 \pm 1.070	5.750 \pm 2.830	4.312 \pm 2.732	7.360 \pm 4.840	7.275 \pm 4.840				
p1a4	11 18 21.515	-32 49 09.27	7.0	0.661 \pm 0.124	0.584 \pm 0.093	3.560 \pm 0.295	8.960 \pm 0.769	7.097 \pm 0.725	29.800 \pm 1.460	29.691 \pm 1.460				
s3a2	11 18 30.554	-32 48 47.33	6.0	0.034 \pm 0.004	0.021 \pm 0.003	0.027 \pm 0.012	0.067 \pm 0.022	0.046 \pm 0.021	0.087 \pm 0.050	0.082 \pm 0.050				
s3a1	11 18 30.425	-32 48 34.15	5.0	0.013 \pm 0.004	0.011 \pm 0.003	0.081 \pm 0.012	0.159 \pm 0.029	0.122 \pm 0.027	0.561 \pm 0.068	0.559 \pm 0.069				
NGC 6946														
NGC 6946-2	20 34 34.935	+60 11 38.62	6.0	0.965 \pm 0.143	0.833 \pm 0.113	6.040 \pm 0.791	15.000 \pm 1.960	11.659 \pm 1.856	32.100 \pm 3.290	31.959 \pm 3.290				
NGC 6946-6	20 34 52.435	+60 10 18.56	6.0	0.131 \pm 0.140	0.078 \pm 0.088	0.539 \pm 0.305	1.640 \pm 0.898	0.941 \pm 1.309	0.449 \pm 0.758	0.430 \pm 0.758				
NGC 6946-8	20 34 54.399	+60 10 38.86	6.0	0.542 \pm 0.090	0.489 \pm 0.073	2.680 \pm 0.688	6.720 \pm 1.920	4.985 \pm 1.832	8.610 \pm 1.730	8.531 \pm 1.730				
NGC 6946-10	20 34 58.778	+60 10 50.60	5.0	0.428 \pm 0.099	0.349 \pm 0.071	3.080 \pm 0.446	8.360 \pm 1.200	6.332 \pm 1.153	10.400 \pm 1.620	10.337 \pm 1.620				
NGC 6946-11	20 35 09.377	+60 11 11.30	5.0	0.091 \pm 0.040	0.072 \pm 0.031	0.578 \pm 0.245	1.560 \pm 0.604	1.183 \pm 0.577	2.010 \pm 0.570	1.997 \pm 0.570				
NGC 6946-21	20 34 36.086	+60 11 41.99	6.0	0.795 \pm 0.091	0.672 \pm 0.077	4.520 \pm 0.544	11.200 \pm 1.360	8.628 \pm 1.294	21.500 \pm 2.770	21.384 \pm 2.770				
NGC 6946-23	20 34 55.894	+60 10 56.50	5.0	0.278 \pm 0.122	0.253 \pm 0.090	1.780 \pm 0.577	4.460 \pm 1.510	3.446 \pm 1.429	8.600 \pm 1.480	8.559 \pm 1.480				
NGC 6946-26	20 35 07.970	+60 11 13.01	5.0	0.259 \pm 0.091	0.231 \pm 0.074	1.540 \pm 0.359	3.840 \pm 0.891	2.842 \pm 0.871	4.670 \pm 1.640	4.632 \pm 1.640				
NGC 6946-27	20 35 06.596	+60 11 11.50	6.0	0.335 \pm 0.136	0.339 \pm 0.111	2.760 \pm 0.829	7.340 \pm 2.100	5.613 \pm 2.015	10.700 \pm 3.690	10.651 \pm 3.690				
NGC 6946-30	20 35 16.805	+60 11 00.39	9.0	0.959 \pm 0.748	0.834 \pm 0.592	8.690 \pm 1.440	22.800 \pm 1.890	18.171 \pm 1.819	61.500 \pm 1.370	61.360 \pm 1.374				
NGC 6946-32	20 35 19.315	+60 10 46.27	4.0	0.066 \pm 0.019	0.053 \pm 0.014	0.298 \pm 0.070	0.720 \pm 0.179	0.502 \pm 0.176	0.609 \pm 0.154	0.599 \pm 0.154				
NGC 6946-34	20 34 45.728	+60 08 20.58	4.0	0.123 \pm 0.047	0.097 \pm 0.038	0.722 \pm 0.263	1.900 \pm 0.662	1.481 \pm 0.630	3.670 \pm 1.410	3.652 \pm 1.410				
NGC 6946-36	20 34 54.574	+60 07 39.80	7.0	0.863 \pm 0.149	0.719 \pm 0.108	5.450 \pm 0.554	13.900 \pm 1.420	10.798 \pm 1.344	27.400 \pm 1.510	27.274 \pm 1.510				
NGC 6946-39	20 35 05.107	+60 07 03.53	7.0	0.100 \pm 0.023	0.071 \pm 0.017	0.649 \pm 0.117	1.810 \pm 0.328	1.245 \pm 0.325	1.080 \pm 0.184	1.065 \pm 0.184				

Table 4: Parameters of H II complexes: designation, age, metallicity estimated by ‘ONS’ method (except for Holmberg II where the ‘NS’ method is used) and the ratio $[O III]\lambda 5007/H\beta$ considered as a potential indicator of the radiation field hardness

Object	age, Myr	$12+\log(O/H)$	$[O III]\lambda 5007/H\beta$
IC 1727			
IC 1727_3	5.16 ± 0.25	8.01 ± 0.02	1.77 ± 0.26
IC 1727_5	4.99 ± 0.24	8.03 ± 0.03	1.50 ± 0.06
IC 1727_6	4.88 ± 0.24	8.02 ± 0.06	1.48 ± 0.09
IC 1727_9	6.85 ± 0.27	7.93 ± 0.10	1.26 ± 0.21
IC 1727_10	3.89 ± 0.18	8.05 ± 0.03	2.32 ± 0.24
IC 1727_11	3.79 ± 0.17	8.11 ± 0.14	3.80 ± 0.19
NGC 7741			
NGC 7741_1	5.18 ± 0.15	8.13 ± 0.06	1.78 ± 0.36
NGC 7741_3	6.56 ± 0.31	8.49 ± 0.01	0.72 ± 0.48
NGC 7741_4	7.55 ± 0.37	8.37 ± 0.03	0.85 ± 0.08
NGC 7741_7	6.58 ± 0.31	8.28 ± 0.11	0.87 ± 0.08
NGC 7741_9	8.55 ± 0.25	8.35 ± 0.05	1.76 ± 0.12
NGC 7741_10	6.55 ± 0.42	8.32 ± 0.06	2.83 ± 0.36
Holmberg II			
HSK 7	3.69 ± 0.14	7.76 ± 0.03	4.25 ± 0.18
HSK 15	5.21 ± 0.14	7.63 ± 0.10	1.60 ± 0.08
HSK 16-17	5.59 ± 0.15	7.68 ± 0.05	2.06 ± 0.07
HSK 20	5.73 ± 0.16	7.45 ± 0.04	1.01 ± 0.10
HSK 25	6.64 ± 0.18	7.53 ± 0.02	1.13 ± 0.02
HSK 31	6.38 ± 0.18	7.97 ± 0.12	3.29 ± 0.04
HSK 59	3.83 ± 0.12	7.60 ± 0.03	1.82 ± 0.02
HSK 61	7.81 ± 0.22	7.66 ± 0.03	2.06 ± 0.03
HSK 67	3.74 ± 0.11	7.57 ± 0.02	2.97 ± 0.02
HSK 70	4.82 ± 0.14	7.77 ± 0.02	2.93 ± 0.02
HSK 71-73	3.58 ± 0.10	7.73 ± 0.03	2.23 ± 0.02
IC 2574			
IC 2574-1	3.41 ± 0.10	7.72 ± 0.03	4.41 ± 0.33
IC 2574-2	4.21 ± 0.13	7.78 ± 0.03	2.69 ± 0.20
IC 2574-3	2.71 ± 0.08	7.82 ± 0.03	4.69 ± 0.35
IC 2574-5	4.03 ± 0.12	7.81 ± 0.04	4.57 ± 0.34
IC 2574-6	3.97 ± 0.12	7.77 ± 0.03	4.12 ± 0.31
IC 2574-8	3.93 ± 0.12	7.80 ± 0.03	4.15 ± 0.31
IC 2574-9	4.66 ± 0.14	7.85 ± 0.06	3.46 ± 0.26
IC 2574-10	5.06 ± 0.14	7.72 ± 0.04	3.70 ± 0.28
IC 2574-11	4.53 ± 0.14	7.80 ± 0.15	2.64 ± 0.20
IC 2574-13	4.36 ± 0.14	7.76 ± 0.15	3.71 ± 0.28
IC 2574-14	5.82 ± 0.15	7.79 ± 0.15	3.92 ± 0.30
NGC 628			
NGC 628-7	3.37 ± 0.23	8.41 ± 0.04	0.49 ± 0.07
NGC 628-8	4.43 ± 0.29	8.45 ± 0.02	0.66 ± 0.07
NGC 628-10	4.88 ± 0.35	8.37 ± 0.12	0.36 ± 0.10
+081-140	4.61 ± 0.31	8.46 ± 0.03	1.11 ± 0.03
+062-158	4.55 ± 0.32	8.60 ± 0.03	0.26 ± 0.04
+047-172	5.00 ± 0.34	8.51 ± 0.01	0.77 ± 0.03
+044-175	3.24 ± 0.22	8.48 ± 0.01	1.54 ± 0.05
+178-052	3.88 ± 0.26	8.46 ± 0.04	0.85 ± 0.03
-086+186	3.21 ± 0.22	8.50 ± 0.01	1.54 ± 0.04
-075+200	4.86 ± 0.33	8.48 ± 0.01	1.10 ± 0.05
NGC 925			
+042-011	5.01 ± 0.33	8.42 ± 0.01	0.95 ± 0.03
+135-016	5.06 ± 0.21	8.16 ± 0.02	2.02 ± 0.06
+087-031	4.41 ± 0.28	8.36 ± 0.01	1.70 ± 0.05
-012-066	2.57 ± 0.11	8.27 ± 0.01	3.82 ± 0.12
-047-058	4.79 ± 0.31	8.32 ± 0.01	1.15 ± 0.04
-137+056	3.03 ± 0.20	8.40 ± 0.01	1.79 ± 0.05
-080+087	3.94 ± 0.26	8.32 ± 0.01	1.45 ± 0.04
-114+087	5.94 ± 0.25	8.21 ± 0.02	1.98 ± 0.06
-198-013	3.77 ± 0.15	8.13 ± 0.02	3.41 ± 0.10
-220+004	3.67 ± 0.17	8.28 ± 0.01	1.49 ± 0.04
+156-114	4.07 ± 0.17	8.27 ± 0.01	1.65 ± 0.05
+206-114	4.31 ± 0.17	8.09 ± 0.01	2.22 ± 0.07
+019+143	3.80 ± 0.15	8.07 ± 0.02	4.43 ± 0.14
-250+019	3.35 ± 0.14	8.21 ± 0.01	2.92 ± 0.09
-274+010	5.03 ± 0.21	8.17 ± 0.02	2.87 ± 0.09
-174+140	5.28 ± 0.22	8.10 ± 0.02	2.74 ± 0.09
-159+162	5.61 ± 0.22	8.03 ± 0.02	0.99 ± 0.05
-149+177	4.81 ± 0.27	7.99 ± 0.02	1.40 ± 0.04
-262+011	5.12 ± 0.21	8.11 ± 0.03	1.97 ± 0.09
NGC 3184			
-058-007	5.67 ± 0.90	8.78 ± 0.01	0.08 ± 0.01
-064-006	5.36 ± 0.85	8.70 ± 0.01	0.14 ± 0.02
-080-005	4.96 ± 0.34	8.68 ± 0.01	0.17 ± 0.01
+085-004	0.10 ± 0.01	8.65 ± 0.01	0.17 ± 0.02
+079+035	4.97 ± 0.79	8.72 ± 0.01	0.10 ± 0.01
+074+064	6.80 ± 0.46	8.61 ± 0.01	0.29 ± 0.03
+059-079	5.12 ± 0.35	8.65 ± 0.01	0.14 ± 0.01
+092-093	4.52 ± 0.32	8.64 ± 0.01	0.15 ± 0.01
+111-102	6.78 ± 0.46	8.43 ± 0.02	0.81 ± 0.10
+005+135	4.71 ± 0.32	8.48 ± 0.01	0.78 ± 0.02
-017+137	3.48 ± 0.23	8.59 ± 0.01	0.26 ± 0.01
NGC 3621			
s5a2	4.94 ± 0.33	8.45 ± 0.03	1.45 ± 0.20
s5a1	4.38 ± 0.30	8.52 ± 0.02	0.60 ± 0.08
p1a8	6.20 ± 0.40	8.51 ± 0.05	0.65 ± 0.23
p2a6	4.76 ± 0.33	8.63 ± 0.05	0.21 ± 0.07
p1a9	3.14 ± 0.21	8.37 ± 0.09	2.13 ± 0.22
p2a7	4.68 ± 0.31	8.47 ± 0.02	1.17 ± 0.12
p1a7	3.14 ± 0.21	8.47 ± 0.02	0.66 ± 0.07
p1a6	2.19 ± 0.16	8.53 ± 0.03	0.37 ± 0.11
p2a5	4.36 ± 0.32	8.69 ± 0.06	0.10 ± 0.05
p1a5	5.10 ± 0.84	8.91 ± 0.05	0.02 ± 0.01
p2a4	5.60 ± 0.37	8.60 ± 0.03	0.20 ± 0.05
p1a3	3.02 ± 0.21	8.51 ± 0.04	1.49 ± 0.22
s1a4	3.35 ± 0.23	8.38 ± 0.02	2.53 ± 0.25
p2a2	4.67 ± 0.31	8.45 ± 0.02	0.93 ± 0.10
s2a2	4.86 ± 0.33	8.46 ± 0.02	0.69 ± 0.07
p2a1	4.21 ± 0.28	8.46 ± 0.01	0.95 ± 0.17
p1a2	5.48 ± 0.37	8.40 ± 0.02	2.01 ± 0.20
s2a3	5.29 ± 0.35	8.60 ± 0.02	0.19 ± 0.03
p1a4	4.53 ± 0.30	8.47 ± 0.02	1.15 ± 0.11
s3a2	5.20 ± 0.35	8.49 ± 0.02	2.59 ± 0.26
s3a1	4.81 ± 0.32	8.41 ± 0.01	2.29 ± 0.23
NGC 6946			
NGC 6946-2	4.47 ± 0.30	8.47 ± 0.01	0.79 ± 0.03
NGC 6946-6	7.26 ± 0.49	8.59 ± 0.02	0.35 ± 0.04
NGC 6946-8	4.75 ± 0.33	8.60 ± 0.01	0.29 ± 0.01

Table 4: Parameters of H II complexes: designation, age, metallicity estimated by ‘ONS’ method (except for Holmberg II where the ‘NS’ method is used) and the ratio $[O\ III]\lambda 5007/H\beta$ considered as a potential indicator of the radiation field hardness

Object	age, Myr	$12+\log(O/H)$	$[O\ III]\lambda 5007/H\beta$
NGC 6946-10	6.35 ± 1.03	8.76 ± 0.05	0.04 ± 0.02
NGC 6946-11	4.41 ± 0.32	8.69 ± 0.02	0.07 ± 0.02
NGC 6946-21	3.93 ± 0.26	8.41 ± 0.01	0.31 ± 0.02
NGC 6946-23	4.60 ± 0.31	8.47 ± 0.01	0.63 ± 0.04
NGC 6946-26	5.37 ± 0.36	8.37 ± 0.01	0.74 ± 0.03
NGC 6946-27	4.37 ± 0.28	8.35 ± 0.01	0.95 ± 0.03
NGC 6946-30	4.55 ± 0.29	8.38 ± 0.01	2.02 ± 0.05
NGC 6946-32	6.57 ± 0.44	8.40 ± 0.02	1.56 ± 0.11
NGC 6946-34	5.76 ± 0.38	8.67 ± 0.02	0.19 ± 0.03
NGC 6946-36	6.39 ± 0.43	8.32 ± 0.01	0.08 ± 0.02
NGC 6946-39	4.57 ± 0.33	8.65 ± 0.01	0.15 ± 0.01